

Proceedings of

SSBE Annual Meeting 2017



Scientific Annual Meeting of the Swiss Society for Biomedical Engineering
August, 30, ZHAW, Winterthur

Proceedings of the Annual Meeting of the Swiss Society for Biomedical
Engineering

© Swiss Society for Biomedical Engineering, 2017

www.ssbe.ch

Contents

Programme

Abstracts

Technology Management in a Clinical Environment (G. Lutters)

Big Data – A perspective for biomedical engineering (S. Hirsch)

Patient Big Data – An analysis integrating medical images, molecular profiles and physical activity levels (Nicholas Ohs)

A relaxing virtual reality setup to stimulate patients in the intensive care unit: a proof-of-concept (S. Gerber)

Patient specific interventions based on long-term ambient and wearable sensor data (N. Schutz)

Open-source low-cost wearable physical activity tracker (J. Dragas)

Comparing single- and double-grating hard X-ray phase tomography for soft tissue visualization (P. Thalmann)

Tomographic imaging and computational analysis of brain structures in subcellular detail (S.E. Hieber)

Cell lacunar imaging dependence on μ CT beam energy (E. Goff)

Comparison between intraoperative and chronic deep brain stimulation (D. Vogel)

Thermal cameras enhance ROI detection in photoplethysmographic imaging (G. Scebba)

Automatic segmentation of the knee joint in MRI data (A. Ringenbach)

Lumen determination in plaque-containing vessels (M. Buscema)

Laboratory micro computed tomography for the visualization of the mouse brain (C. Bikis)

Imaging cellular structure of human brain tissue using micro computed tomography (A. Khimchenko)

Phase tomography using laboratory sources to visualise cartilage of human knee (G.Schulz)

Precision measurements of oral scanners (C. Vögtlin)

Multi-center abdominal CT protocols: A phantom study on image quality and radiation dose levels (D. Racine)

Multi-modality sensory feedback system for upper limb amputees (H. Huang)

A wearable system for multichannel bioimpedance ECG monitoring (M. Rapin)

Manipulation of single neurons and defined neural circuits with force-controlled nanopipette (I. Lüchtfeld)

Fluid FM: A platform for 3D additive manufacturing of metal structures at the micron scale (C.A.J. van Nisselroy)

Sideway-fabricated SU-8 hollow cantilevers and applications (H. Han)

Real-time measurement of glucose concentration in 3D culture of human intervertebral disc cells (D.A. Frauchiger)

Three-dimensional magnetic camera for biomedical applications (J. Pascal)

A wireless sensor for measurement of soft tissue strains in vivo (Q. Zhang)

Incubator temperature calibration and monitoring for hyperthermia in-vitro experiments (M. Weyland)

Multiscale 3D data visualization for the exploration of bone mechanomics (A.C. Scheuren)

Investigating local mechanical regulation of bone healing in an in vivo mouse femoral defect model (D. C. Betts)

Walking comparison between partial and total knee arthroplasty using a moving fluoroscope (T. Zumbrunn)

Kinematics analysis of partial knee implants: in vivo comparison of different activities (A. Roth)

Kinetics of medial unicompartmental knee arthroplasty: comparison to contralateral leg (L. Suter)

Validation of videofluoroscopy technique for kinematic analysis of partial knee implants (L. Kiener)

Finite element modeling of a trochleodysplastic knee: stress distribution in the patellofemoral joint (T. Götschi)

Identifying the role of focal adhesions and the nucleus in cellular tensile stiffness: A finite element approach (A. Horvath)

Stimulation of primary human osteoblasts with the BMP antagonists noggin, gremlin1/2 and chordin (R. D. May)

Minimising external fixator stiffness variation via computational analysis (G. R. Paul)

Computational fluid dynamics modelling of stented coronary arteries (P. Bischof)

Soft and nano-structured metal electrodes for flexible electronics (B. Osmani)

Artificial muscles to treat severe incontinence (B. Müller)

A novel biomimetic in vitro model to study osteocyte mechanobiology using micro-3D printing (F.R. Flohr)

Mechanical and biological characterization of 3D printed polymer lattices for bone tissue engineering (P.F. Egan)

Optimization of 3D printed hydrogels with primary anterior cruciate ligament cells for tissue engineering (E. Bakirci)

Finite element simulation for 3D printed scaffolds (X. Wang)

Adverse immune effects to artificial, shear-responsive liposomes (S. Matviyukiv)

Characterization of shear-responsive liposomes using microfluidics and small-angle x-ray scattering (Thomas Pfohl)

Template stripping based nanotransfer printing of plasmonic gold structures for biosensing applications (R.F. Tiefenauer)

Fabrication of nano-structured dielectric elastomer transducers for medical implants (T. Töpfer)

Lung microvasculature-on-chip: in vitro microfluidic platform for drug testing (S. Zeinali)

Development of a lung alveoli array-on-chip with a collagen-elastin membrane (P. G. V. Zamprogno)

An integrated electrospray generator for gene delivery (C. Minonzio)

Author Index

Programme

	Physics Building TP 406	Laboratory Building TL 201
0830-0900	Welcome Coffee and Registration TP Entrance / Foyer	
0900-0915	Welcome and Opening	
0915-1015 1015-1042	Key Note Talks Session A (Plenary Session): Medical Systems & Medical Data	
1045-1100	Coffee Break / Poster Viewing	
1100-1220	Session B (Plenary Session): Imaging & Image Guided Therapies	
1220-1330	Lunch (Mensa TB)	
1330-1400	SSBE General Assembly	
1400-1410	Short break / leg stretch	
1410-1510	Session C (Parallel Session): Sensors & Signals	Session D (Parallel Session): Biomechanics
1510-1540	Poster Session /Break / Refreshing (TP Foyer)	
1540-1650	Session E (Plenary Session): Biomaterials, Micro- & Nano-Technology, Tissue Engineering	
1650-1750	SSBE Awards	
1800-2000	Apéro / Dinner (TB Building)	

PATIENT BIG DATA – AN ANALYSIS INTEGRATING MEDICAL IMAGES, MOLECULAR PROFILES AND PHYSICAL ACTIVITY LEVELS

Nicholas Ohs (1), Jan Kleffmann (1), Yuk-Wai Wayne Lee (2), Chun-Yiu Jack Cheng (2), Peter Arbenz (3), Ralph Müller (1), Patrik Christen (1)

1. Institute for Biomechanics, ETH Zurich, Zurich, Switzerland; 2. Department of Orthopaedics & Traumatology, The Chinese University of Hong Kong, Hong Kong SAR, China; 3. Computer Science Department, ETH Zurich, Zurich, Switzerland

Introduction

The advancement in clinically relevant big data acquisition and analysis emerges to provide a solution to the clinical challenge of accurate prognostication of complex trait diseases to allow timely treatments. Bone metabolism is a dynamic biological process affected by internal and external factors, which could possess significant impact for various pathological conditions. Apart from common osteoporotic problems, recent evidence suggests that low bone mass and deranged structure could be prognostic factors for curve progression of adolescent idiopathic scoliosis (AIS). AIS is a prevalent three dimensional spinal deformity (2-4% worldwide) during the pubertal growth period without clear aetiology and pathogenesis. Genetic and epigenetic anomalies [Cheng, 2015], reduced physical activity [Lee 2005], and vitamin D insufficiency are reported associations. The current understanding on how bone metabolism affects AIS was mainly gained from serological and cellular studies which could not delineate the complicated interactions of various factors. We here propose a simulation based medical data science framework to prognosticate bone loss associated with AIS in a first prototype based on patient big data potentially providing insight into the pathogenesis of AIS in the future.

Methods

A cellular automaton (CA) was used to integrate medical image data, micro-finite element analysis to integrate physical activity levels, and a Boolean network to integrate molecular and hormone profiles into a simulation based medical data science framework for the integrated analysis of patient big data. All the inputs were linked with the update rule of the cellular automaton (Fig. 1). The Boolean networks model molecular interaction on a per image voxel basis either with available molecular images or in our prototype via statistical distributions of global measurements [Ohs, 2016]. A Python interface was developed that allows organising large numbers of simulations that works on a desktop system as well as on a supercomputer.

Results

In the AIS prototype, high-resolution peripheral quantitative computed tomography (HR-pQCT) medical images of the distal tibia, physical activity levels, and circulating vitamin D and parathyroid hormone (PTH) levels were integrated. Personalised bone health prognosis of an AIS patient with normal physical activity and patient-specific vitamin D and PTH levels showed minor changes in bone mass whereas the prognosis with reduced physical activity of the same patient led to reduced bone mass.

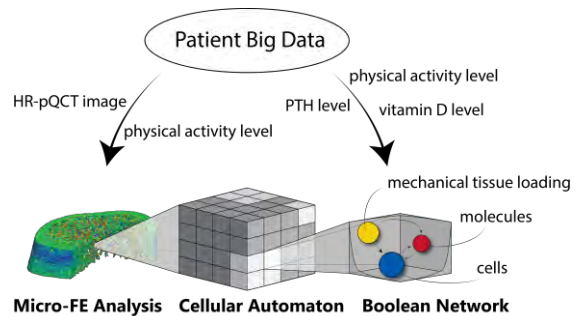


Figure 1: Patient big data are integrated into different parts of the simulation based medical data science framework.

Conclusion

We conclude that our simulation based medical data science framework allows the integrated patient big data analysis accounting for a variety of data types, especially imaging, molecular, hormonal, and physical activity data to study complex trait diseases and to perform personalised bone health prognosis. Due to the Python interface, future studies will benefit from having the ability to perform a large number of large-scale simulations.

References

- Cheng et al., Nature Review Disease Primers, 1, 2015.
- Lee et al., Osteoporosis International, 16:1034-1035, 2005.
- Ohs et al., Current Directions in Biomedical Engineering, 2:57-60, 2016.

A RELAXING VIRTUAL REALITY SETUP TO STIMULATE PATIENTS IN THE INTENSIVE CARE UNIT: A PROOF-OF-CONCEPT

Stephan Gerber (1), Marie-Madlen Jeitziner (2), Patric Wyss (1), Alvin Chesham (1), Prabitha Urwyler (1,3), René Mürli (1,4), Stephan Jakob (2) & Tobias Nef (1,5)

1 Gerontechnology & Rehabilitation Group, University of Bern, Switzerland;
2 Department of Intensive Care Medicine, Inselspital, University of Bern, Switzerland;
3 University Hospital of Old Age Psychiatry, University of Bern, Switzerland;
4 Department of Neurology, Inselspital, University of Bern, Switzerland;
5 ARTORG Center for Biomedical Engineering Research, University of Bern, Switzerland

Introduction

Around 70% of patients in the intensive care unit (ICU) suffer from long-term functional deficits after prolonged stay in the ICU, resulting in a reduction of quality of life (Wergin 2012, Wilcox 2013). It is assumed that the noisy and stressful ICU environment leads to both stimulus habituation and deprivation in patients which in turn causes cognitive impairment (Tainter, 2016). The activation of attention through stimulation seems to support patients in their cognitive functions and their environmental relationship (Pickenhain, 1988). The aim of this proof-of-concept study was to measure the effect of audio-visual virtual reality (VR) stimulation on eye movement and physiological data in healthy volunteers in an ICU setting.

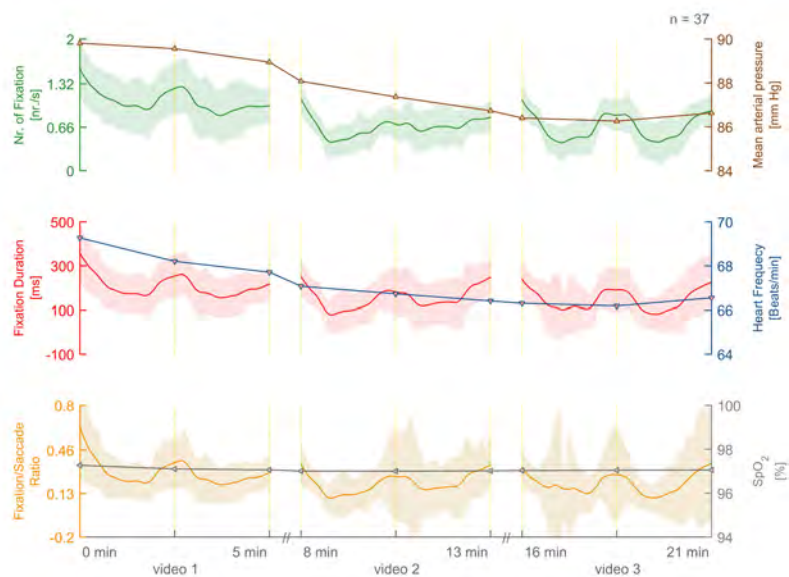


Figure 1. Pooled eye- and vital data of the control group ($n=37$, age = 48 ± 17 years).

Method:

The VR procedure consisted of a head-mounted display (Oculus Rift DK2, Facebook) that isolated patients from disturbing environmental audio- and visual input in combination with an eye tracker to measure eye movements and sensors to assess physiological parameters which was tested on 37 healthy subjects (age = 48 ± 17 years). The VR stimulation featured three immersive nature sceneries, each five minutes in length, with a break between videos. In each video a target (emoticon) was presented three times.

Results:

Heart frequency ($p < 0.001$) and blood pressure ($p < 0.001$) significantly decreased during the audio-visual stimulation except of the peripheral capillary oxygen saturation (SpO_2 , $p = 0.501$) which remained constant, shown in figure 1. However, the decrease in eye movement data over time was very small and not significant. Fixation/saccade ratio was decreased when no visual target was presented,

reflecting enhanced visual search and reduced visual processing.

Conclusion:

Overall stimulation had a strong relaxing and calming effect and did not evoke any negative reactions like sickness. Since immersion was at a high level, the participants were not aware of their surroundings. Furthermore, during stimulation, the visual search activity was reduced when given attention to a target, compared to the other parts of the video. In this study we pointed out that VR stimulation in ICU settings is feasible and beneficial for critically ill patients.

References

- Wergin, R. & Modrykamien, *Cleveland Clinic journal of medicine*, 2012
- Wilcox, M. E. et al., *Critical care medicine*, 2013
- Tainter, C. R. et al, *Critical care medicine*, 2016
- Pickenhain et al., *Advances in psychology*, 1988

PATIENT SPECIFIC INTERVENTIONS BASED ON LONG-TERM AMBIENT AND WEARABLE SENSOR DATA

Narayan Schutz (1), Prabitha Urwyler (1,2), Hugo Saner (1,3), Tobias Nef (1,4)

1. Gerontechnology and Rehabilitation, University of Bern, Switzerland; 2. University Hospital of Old Age Psychiatry, University of Bern, Switzerland; 3. University Clinic of Cardiology, University Hospital Bern, Inselspital, Switzerland; 4. ARTORG Center for Biomedical Engineering, University of Bern, Switzerland

Introduction

In our aging society, prolonged independent living of older people is not only a question of individual preference but also an economical one. A study from OBSAN [Weavre, 2008] showed, that increasing home care in comparison to institutionalisation, may have a significant effect in lowering health-care cost projections. Additionally, it is obvious that most seniors want to age in their well-known environment for as long as possible.

Often assessing the actual health-state – be it mental or physical – is based on self-reporting, [Rosenman, 2011] which may be highly subjective and thus result in a response bias. New sensor technology could provide an objective alternative to ordinary evaluations forms – such as questionnaires. In this study, we want to investigate whether sensor technology could not only increase safety through the automatic detection of serious events, like falls, but also enable better tailored care by providing objective health-status information.

Methods

Forty six participants (> 70 years, living alone) have been recruited and will be measured throughout a year, using a set of wearable and ambient sensors. Wearable sensors include a mobile ECG (Preventice Health-Guardian) and a Fitness Watch (FitBit) for 50% of the participants, while the other 50% of participants will be provided with an armband (Biovotion Everion) and an accelerometer (Axivity AC3). Ambient sensors include motion and door sensors (Domo-Safety System) as well as a bed sensor. Simultaneously, questionnaires and muscle strength measures will be recorded, while local caregivers will visit the participants twice a week to get information about lifestyle changes, accidents and other unforeseeable events.

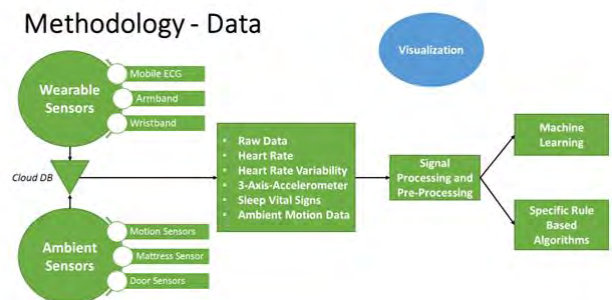


Figure 1: Methodology used in the study.

Outlook

We aim to combine different algorithms such as activities of daily living detection (ADL), stress-recognition or anomaly detection towards building models that can effectively evaluate the current health state and ideally give some predictive information about future states.

Acknowledgements

This study is funded as a CTI project, in collaboration with Domo-Safety SA. We thank local health-care institutions, namely Ecole La Source (Lausanne), NOMAD (Neuchâtel) and BBZ Olten for their help in recruiting and service towards patients.

References

- Weavre et al, Swiss Health Observatory, 34:58-72, 2008.
- Rosenman et al, Int J Behav Health Res, 2:320-332, 2011

OPEN-SOURCE LOW-COST WEARABLE PHYSICAL ACTIVITY TRACKER

Jelena Dragas and Walter Karlen

*Mobile Health Systems Lab, Institute of Robotics and Intelligent Systems,
Department of Health Sciences and Technology, ETH Zurich, Zurich, Switzerland*

Introduction

Physical inactivity is one of the most important risk factors affecting global health [WHO, 2015]. Physical activity and good sleep reduce occurrences of cardiac [Yusuf, 2004], bone and joint diseases [Warburton, 2006], and are linked to occurrences of diabetes [Lee, 2016] and Alzheimer's [Spira, 2013]. Long-term tracking of physical activity could help in early detection of emerging senescence [Fried, 2001] as well as help track the progress of rehabilitation in patients.

Devices used for tracking physical activity in clinical settings are too expensive for ubiquitous and long-term use, while low-cost consumer devices fail to replicate the performance of their clinical counterparts. Furthermore, commercially available devices lack transparency in data processing, and hence, limit their suitability for conducting objective research.

Methods

We have developed a low-cost physical activity tracking platform consisting of a 3-axis accelerometer module and a mobile app (Fig). The wearable device can be wirelessly configured with algorithms optimized for a particular type of physical activity and sensor placement (e.g., wrist, waist, ankle). Device hardware and algorithms are open-sourced to offer maximal transparency. The device features an exchangeable coin battery and 16 MB internal memory, offering up to 6 months of standalone operation. Additionally, the data can be streamed via Bluetooth to the mobile app.

Results

The open-source hardware and software allow for developing novel applications and configuring the device with customized, user-specific algorithms. The open-source design enables novel research and citizen-science applications, as well as device personalization, which is particularly useful in clinical use. The low cost device offers possibility of conducting a wide-range of studies and wide-range patient monitoring in, e.g., course of rehabilitation or early diagnostics of emerging senescence.

Real-time data streaming to a secure data server offers the possibility for the clinicians to remotely track the patient's activity. Moreover, methods for



Figure: Actimeter prototype.

an automatic tracking of changes in activity can be implemented in order to reduce clinician's workload.

Discussion

The developed actimeter offers the performance of a clinical-grade device in a price range of a consumer device; this makes it particularly suitable for research and clinical use where full transparency is needed.

References

- Fried et al, J. Gerontol., Ser. a: Biol. Sci. Med. Sci., 56: 146-156, 2001.
- Lee et al, Sleep Med. Rev., 31:91-101, 2016.
- Spira et al, JAMA Neurol., 70(12):1537-43, 2013.
- Warburton et al, J. Can. Med. Assoc., 174:801-809, 2006.
- WHO Global Burden of Disease Study, 2015.
- Yusuf et al, Lancet, 364:937-952, 2004.

COMPARING SINGLE- AND DOUBLE-GRATING HARD X-RAY PHASE TOMOGRAPHY FOR SOFT TISSUE VISUALIZATION

Peter Thalmann (1), Christos Bikis (1), Alexander Hipp (2), Hans Deyhle (1), Felix Beckmann(2), Simone E. Hieber (2), Bert Müller(1), Georg Schulz (1)

1. Biomaterials Science Center, Department of Biomedical Engineering, University of Basel, Basel, Switzerland; 2. Institute of Materials Research, Helmholtz-Zentrum Geesthacht, Germany

Introduction

For the visualization of tissues consisting of low absorbing elements at microscopic level, hard X-ray phase tomography has been proposed. Double-grating interferometry (XDGI) is often used for the visualization of soft tissues, including human brain tissue [Schulz 2010], due to the superior contrast achieved. Recently, smaller detector elements have allowed for the direct resolution of the interference pattern generated by gratings with micrometer-sized periods. Therefore, the analyser grating becomes superfluous. Such a single-grating interferometer (XSGI) setup benefits from easier handling, as only one grating has to be aligned. Most importantly, the spatial resolution for the XSGI is no longer limited by the analyser grating period and for equal flux the number of detected photons is increased by a factor of about two.

Materials and Methods

Tomography experiments were carried out at the beamline P07 (PETRA III, DESY, Hamburg, Germany), operated by the HZG [Hipp 2014] using a photon energy of 40 keV. The XSGI measurement was performed using a $\pi/2$ beam-splitter grating with a periodicity of 4.8 μm . The XDGI measurement consisted of a π beam splitter grating with a periodicity of 4.8 μm and an Au analyser grating with a periodicity of 2.4 μm . The sensitivity and the visibility of both techniques should be similar to allow for a fair comparison. Therefore, the distance between grating and detector for the XSGI was 248 mm -- close to the first fractional Talbot order -- and the inter-grating distance for the XDGI was 496 mm -- close to the third fractional Talbot order [Thalmann 2017]. For the experiments, we used a human peripheral nerve obtained from a donated body *post-mortem*. After extraction from the body, the nerve was fixed in 4% histological-grade buffered formalin and subsequently dehydrated and embedded in a paraffin/plastic polymer mixture, according to standard pathology procedure.

Results

The results showed an increased contrast-to-noise ratio for XDGI over XSGI. The calculated spatial resolution of the XSGI was almost twice as high as for

the XDGI, however, in both cases, the contrast was sufficient to observe the main anatomical features of the nerve as illustrated in Figure 1. Thus, the results confirm that XSGI provides images with higher spatial resolution than XDGI, while contrast-to-noise ratio was higher for XDGI.

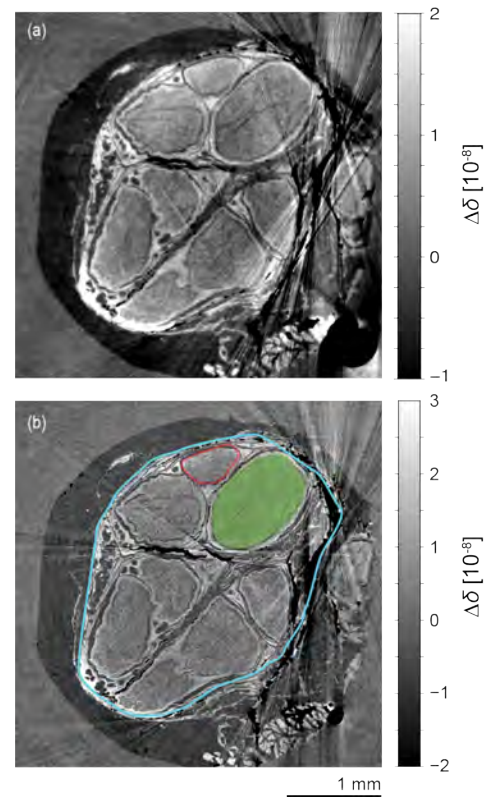


Figure 1: Hard X-ray phase tomography slice of the human nerve using XDGI (a) and XSGI (b). The epineurium (cyan), perineurium (red), and endoneurium (green area) are clearly distinguishable in both slices.

Acknowledgements

The authors thank Georg Schweighauser and Jürgen Hench of the Neuropathology Department of the Basel University Hospital for providing the specimen and helping with the embedding of the sample. The financial support of the Swiss National Science Foundation (Project Nos. 144535 and 147172) is gratefully acknowledged.

References

- G. Schulz et al., J. R. Soc. Interface 7, 1665-1676, (2010)
- A. Hipp et al., Proc. SPIE 9212, 921206, (2014)
- P. Thalmann et al, Appl. Phys. Lett. 110, 061103 (2017)

TOMOGRAPHIC IMAGING AND COMPUTATIONAL ANALYSIS OF BRAIN STRUCTURES IN SUBCELLULAR DETAIL

Simone E. Hieber (1), Christos Bikis (1), Anna Khimchenko (1), Gabriel Schweighauser (2), Jürgen Hench (2), Natalia Chicherova (1,3), Georg Schulz (1), Bert Müller (1)

1. Biomaterials Science Center, Dept. Biomed. Eng., University of Basel, Switzerland;
2. Institute of Pathology, Dept. Neuropathology, University Hospital of Basel, Switzerland;
3. Medical Image Analysis Center, Dept. Biomed. Eng., University of Basel, Switzerland

Introduction

Imaging the human brain on the cellular level has always been a challenge in three dimensions. *In-vivo* methods are hindered by their restricted spatial resolution and three-dimensional microscopy can only penetrate the tissue to limited depth, while the slide thickness of extensive serial sectioning is at best several micrometers. Hard X-ray phase tomography combined with advanced computational analysis offers a promising method to visualize and quantify soft tissue without the application of staining protocols or contrast agents enabling a reliable tissue evaluation in three dimensions [Lang, 2014]. Here, we present the pipeline from specimen preparation via X-ray phase contrast imaging to cell identification for the human cerebellum for the analysis down to the nucleolar level [Hieber, 2016].

Methods

Post mortem specimens of a human cerebellum were excised with informed consent and approved by the Ethikkommission Nordwestschweiz. Two cylindrical parts of the human brain with a height of 4 mm and 2.6 and 6.0 mm in diameter were extracted from the paraffin-embedded specimens. Phase-contrast, single-distance propagation-based X-ray tomography experiments were performed in local configuration. The larger specimen was scanned at the beamline ID 19 (ESRF, Grenoble, France) and the smaller one at Diamond Manchester Imaging Branchline I13-2 (Diamond Light Source, Didcot, UK) with pixel sizes of 1.75 and 0.45 μm , respectively. For the automatic cell identification, we developed and applied an extension of three-dimensional data filter for vessel structures [Frangi, 1998].

Results

The tomograms representing volumes of 43 mm^3 and 2 mm^3 show the characteristic anatomical brain structures including *stratum moleculare*, *stratum granulosum* and the Purkinje cells validated by histology. We automatically identified 5,000 Purkinje cells with an error of less than 5% and determined the average volume and surface density to be 116 per mm^3 and 165 per mm^2 , respectively.

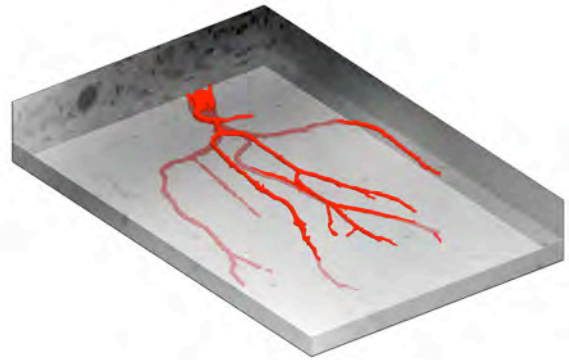


Figure 1: Purkinje cell with dendritic tree segmented from a phase tomogram using feature-based filter in a domain size of $383 \times 248 \times 54 \mu\text{m}^3$ (pixel size 0.45 μm) [Hieber, 2006].

Figure 1 shows that the three-dimensional data allows for the segmentation of subcellular structures, including the dendritic tree of a Purkinje cell. The dendritic tree elongates significantly more in horizontal than in vertical direction, which is characteristic for this cell type.

Conclusions

The proposed approach allows for the three-dimensional quantification of human brain tissue on the subcellular level. Our results suggest a versatile methodology to investigate neuronal organization and nucleoli in brain tissue which also has the potential for automatic cell analysis in other tissue types and beyond.

Acknowledgements

The authors acknowledge the support by the staff at ESRF, Grenoble, France and Diamond Light Source, Didcot, UK. The project was supported by ESRF (proposal MD-861) and by Swiss National Science Foundation projects 147172 and 150164.

References

- Frangi, A. et al, Med Image Comput Comput - Assist Interv 1496: 130 – 137, 1998.
- Hieber, S.E. et al, Sci Rep 6: 32156, 2016.
- Lang, S. et al, J Appl Phys 116: 154903, 2014.

CELL LACUNAR IMAGING DEPENDENCE ON μ CT BEAM ENERGY

Elliott Goff (1), Duncan C Betts (1), Zihui Li (1), Michele Casanova (1), Patrik Christen (1), Ralph Müller (1)

1. Institute for Biomechanics, ETH Zurich, Zurich, Switzerland

Introduction

Osteocytes, the mechanosensing bone cells, live inside individual cave-like structures called lacunae. These lacunae have specific geometries and together they create an intricate network connected via dendritic processes called the lacunocanalicular network (LCN). Detailed analyses of these lacunar structures are now possible with today's highest-resolution micro-CT (μ CT) systems. However, unlike synchrotron μ CT technology, the current standard for imaging small structures such as lacunae [Dong, 2014], there is currently no established imaging protocol for "desktop" μ CT systems with a non-monochromatic X-ray beam. As beam energy affects the linear attenuation coefficient and contrast measured for a given medium, this study was setup to investigate the influence of μ CT beam energy on the detectability of lacunar structures in non-monochromatic μ CT equipment. We hypothesized that just as contrast decreases with increasing energy, the standard deviation of the signal (noise) will also decrease. Furthermore, we asked how this will affect the signal-to-noise ratio (SNR) depending on both terms.

Methods

Six human iliac crest biopsies embedded in PMMA were imaged using a μ CT50 (Scanco Medical, Switzerland) at a nominal voxel resolution of 1.2 μ m. Each sample was scanned at three beam energies: 55, 70, and 90 kVp. The linear attenuation coefficient was measured for ten 2D sub-regions (≈ 0.25 mm²) at each beam energy in three samples (90 regions in total). Signal-to-noise ratio was then calculated by adapting the Firbank equation to account for two materials, where μ is the average coefficient of linear attenuation of bone and the background (PMMA) and σ is the standard deviation of the background [Firbank, 1999].

$$\text{SNR} = 0.655 \frac{\mu_{\text{bone}} - \mu_{\text{PMMA}}}{\sigma_{\text{PMMA}}} \quad (1)$$

Manual lacunar detection was performed for twelve 3D sub-volumes (≈ 0.014 mm³) within two samples (six sub-volumes for 55 & 90 kVp beam energy), using the human eye to identify lacunar pores in the image. Three independent observers manually counted lacunae in each sub-volume by moving through the image stack slices using MATLAB (MathWorks, Natick MA, USA). The inter-operator coefficient of variation (IO_{CV}) was calculated to determine inter-operator variability and its dependency on beam energy.

Results

Figure 1 depicts both the linear and exponential relationships between energy, SNR, and energy, contrast & σ_{PMMA} respectively. As expected, contrast decreased inversely proportional to energy as seen in Table 1. Standard deviation also showed a large reduction, meaning that the noise decreased inversely proportional to energy squared, while SNR, as the ratio of both, was less affected, although these differences were significant with the SNR being the highest for the lowest energy. IO_{CV} was lower for low energy although this was not statistically significant.

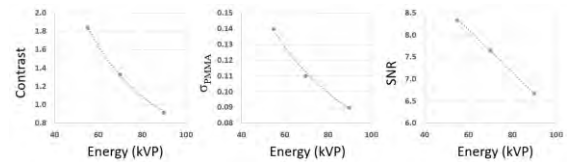


Figure 1: Beam energy relationships.

Energy (kVp)	Contrast (n=30)	σ_{PMMA} (n=30)	SNR (n=30)	IO_{CV} (n=6, %)
55	1.84 \pm 0.46*	0.14 \pm 0.02*	8.34 \pm 2.20*	4.4 \pm 4.0
70	1.33 \pm 0.33*	0.11 \pm 0.01*	7.65 \pm 1.88	N/A
90	0.92 \pm 0.23*	0.09 \pm 0.01*	6.67 \pm 1.60*	7.6 \pm 3.0

Table 1: Energy dependency of μ CT parameters; * $p < 0.005$ between SNR 55&90 and between all three possible combinations in contrast & σ_{PMMA} groups.

Discussion

Contrast and σ_{PMMA} were both dependent on and exponentially related to beam energy. Yet the SNR was linearly related to energy and remained relatively constant. Based on previous literature, these relationships make sense and the exponential nature of contrast and noise could explain the difference in IO_{CV} between 55 & 90 kVp [Edelstein, 1986]. Additionally, from 55 kVp to 90 kVp, standard deviation of the signal dropped by nearly half, thus confirming our hypothesis. Furthermore, 55 kVp also had the most favorable SNR and IO_{CV} for this imaging application and the SNR was significantly better when compared with 90kVp ($p < 0.005$). Based on these findings, we conclude that a lower energy is indeed the better choice to increase SNR and reduce inter-operator variability with respect to the detectability of lacunar structures.

References

- Dong et al, Bone, 60:172-85, 2014.
- Edelstein et al, Magn Reson Med, 3(4):604-618, 1986.
- Firbank et al, Phys. Med. Biol, 44(12):N261, 1999.

COMPARISON BETWEEN INTRAOPERATIVE AND CHRONIC DEEP BRAIN STIMULATION

Vogel D.^{2,1}, Alonso F.¹, Johannes Johansson¹, Simone Hemm-Ode^{2,1}, Karin Wårdell¹

¹Department of Biomedical Engineering, Linköping University, Sweden

²Institute for Medical and Analytical Technologies, School of Life Sciences, University of Applied Sciences and Arts North-western Switzerland, Muttenz, Switzerland

Introduction

Deep Brain Stimulation (DBS) is an established surgical therapy to reduce the symptoms of movement disorders such as Parkinson's disease, Essential Tremor and dystonia. The success of the stimulation depends mainly on the electrode placement precision. To this end, intraoperative Micro Electrode Recoding (MER) is commonly used to locate the optimal stimulation position. However, differences in dimensions and operating modes exist between the exploration and the final DBS electrode which might lead to different stimulation fields, even when ideal placement is achieved. The aim of our investigation is to visualize and compare the electric field (EF) distribution around the intraoperative and the chronic electrode, and evaluate the influence of those differences.

Methods

3D models of the intraoperative exploration electrode and the chronically implanted DBS electrode (3389, Medtronic, USA) were developed using Comsol 5.2 (COMSOL AB, Sweden).

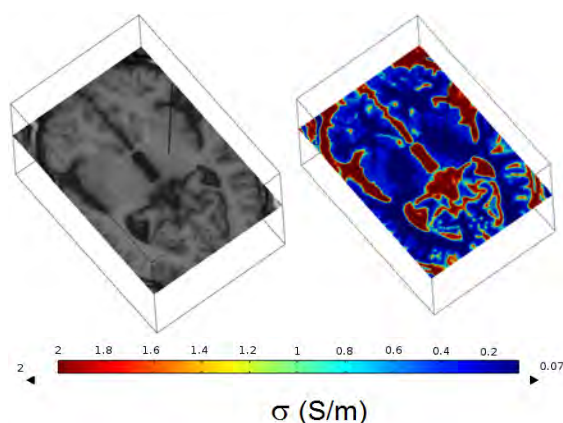


Figure 1: Left: ROI extracted from patient preoperative MRI. Right: patient-specific conductivity model created from the MRI ROI. Both: Slices were taken at the target position.

Patient-specific MRI images were used to determine the conductive medium around the electrode. The MER simulation model included the guide tubes used intra-operatively. The DBS model included the peri-electrode space.

Geometrical and electrical setup followed the DBS implantation procedure used in Clemont-Ferrand University Hospital[1]. Monopolar stimulation was simulated using one contact respectively as current and voltage source for the MER and DBS model; other contacts were left inactive (floating). For the MER model, the guide tubes were set to ground, and for the DBS model, the domain boundaries were used as ground connection. EFs were visualized and compared using 0.2V/mm isocontours. Corresponding values of current and voltage required to achieve the same EF maximal extension were extracted by matching isocontour radial extension.

Results

The EF distribution simulated for the exploration electrode showed the influence of the parallel trajectory and the grounded guide tube. More specifically electric field could be observed around the guide tubes.

Discussion

Differences observed show that electrode geometry and differences in electrical setup modify the population of neurons stimulated intra- and post-operatively. The presence of electric field around the guide tubes and EF distribution alteration, however, require further experimental and clinical evaluation.

References

1. Hemm S, Pison D, Alonso F, Shah A, Coste J, Lemaire JJ, Wårdell K (2016) Patient-Specific Electric Field Simulations and Acceleration Measurements for Objective Analysis of Intraoperative Stimulation Tests in the Thalamus. *Frontiers in human neuroscience* 10:577. doi:10.3389/fnhum.2016.00577

THERMAL CAMERAS ENHANCE ROI DETECTION IN PHOTOPLETHYSMOGRAPHIC IMAGING

Gaetano Scebba, Jelena Dragas, Suyi Hu, Walter Karlen

Mobile Health Systems Lab, Institute of Robotics and Intelligent Systems,
Department of Health Sciences and Technology, ETH Zurich, Zurich, Switzerland

Introduction

Photoplethysmographic imaging (PPGi) enables the estimation of heart rate from RGB video recordings without body contact [Wu, 2000]. PPGi analyses the temporal skin colour change from a region of interest (ROI). Motion artifacts, heterogeneous illumination, and atypical facial characteristics heavily impact the ROI detection and the PPGi signals [Kumar, 2015].

In this work, we investigated if the challenges of motion artifacts and altered ROI areas encountered during the ROI detection could be mitigated by additionally querying a ROI detection from a far-infrared (FIR) camera.

Methods

We implemented three forehead ROI detection algorithms with different input sources [Scebba 2017]: 1) RGB, 2) FIR, and 3) RGB+FIR, which is the combination of two cameras (Figure 1). The forehead was selected as the ROI because of its large exposed and perfused skin area.

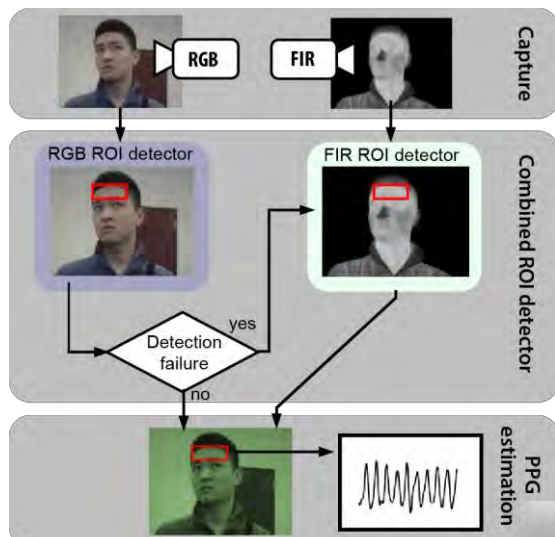


Figure 1: Combined ROI detector: in case the RGB algorithm fails in detecting a ROI, the FIR frame is used. The PPG signal is then estimated by spatial averaging the pixel intensities of the ROI in the green channel.

For evaluating the performance of the ROI detection, we defined the ROI detection rate (% of ROI detected in all frames). This metric quantified the rate of success of detecting a ROI. The algorithms were validated and compared using videos from 8 subjects with distinctively different facial characteristics. The subjects performed three 2 min

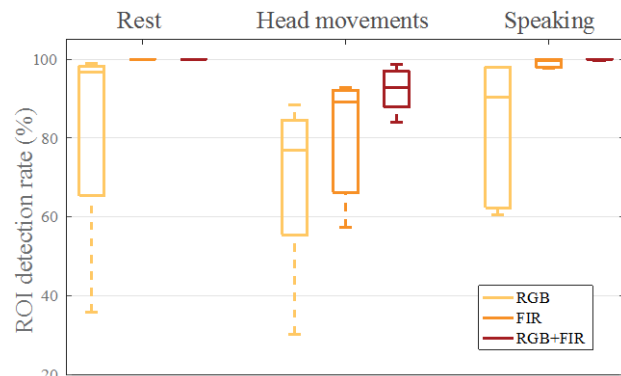


Figure 2: ROI detection rates computed for the RGB, FIR and RGB+FIR algorithms, grouped by task. The boxplots illustrate the distribution across subjects. Middle, bottom, and top horizontal line of the boxes represent median, lower, and upper quartile.

long tasks, each producing a different intensity and type of motion artifact: 1) head at rest, 2) intensive head movements and rotations, and 3) speaking.

Results

Introducing a FIR camera into the system increased the median ROI detection rate at rest from 96.7% (RGB) to 100% (RGB+FIR) (Figure 2). During intensive head movements, the median ROI detection rate increased from 77% (RGB) to 92.8% (RGB+FIR) and during speaking from 90.2% to 100%, respectively.

Discussion

We have presented a novel approach for ROI detection based on the fusion of visible and thermal images. The benefit of fusing multispectral images was most evident during the more challenging task of intensive head movements. The RGB+FIR algorithm clearly outperformed the algorithms using the individual inputs from RGB and FIR cameras.

The adoption of FIR cameras has the potential to improve the reliability of PPGi systems, an important requirement for using contactless vital sign estimation methods in health and medical applications that has not yet been achieved. Further investigation of the robustness and quality of the PPGi signal estimation and its derived vital signs, such as heart and respiratory rate, is required.

References

- Kumar et al, Biomed Opt Express, 6:1565-88, 2015
- Scebba et al, Conf IEEE EMBS, 2017:accepted, 2017
- Wu et al, Proc SPIE , 4163: 67-70, 2000

AUTOMATIC SEGMENTATION OF THE KNEE JOINT IN MRI DATA

Alex Ringenbach¹, Pascal Wettmann²

¹ Institute for Medical and Analytical Technologies, University of Applied Sciences Northwestern Switzerland, Muttenz, CH. ² Medivation AG, Windisch, CH.

Introduction

The production of patient-specific cutting blocks for knee surgery requires a precise segmentation of the knee joint. With an Active Shape Model (ASM) we have realized a fully automatic segmentation of the knee joint, bone and cartilage, in MRI data (gradient echo sequences). With the ASM we use prior knowledge, shape- and texture-information of the object, which makes the segmentation process robust.

Methods

In order to get an Active Shape Model [Coots 2000], we have manually segmented femur and tibia in a set of training data. Then in a first step we have computed a statistical shape model (SSM) for each segment. In a second step we have also captured texture from the training data (at lines perpendicular to the surface) to get the statistical texture information and finally a Mahalanobis classifier at each vertex for value the locally texture.

For the segmentation of an image, we do first a template matching with the mean shape by voting the texture at each position. After we have the position we do a shape adaption with the shape model by the evaluation of the textures in the neighbourhood of each vertex. And for the stability by this optimisation process we include a shape metric (1), which values the shape

$$f(p_i) = \frac{1}{K \alpha^2} \sum_{i=1}^K \left(\frac{p_i}{\sigma_i} \right)^2, \quad (1)$$

in which p_i is the shape parameter, σ_i the standard deviations to the mode i and K is the number of parameters. All this is computed at four different scale levels.

Results

We tested our algorithm on image data captured from different MRI devices and with a high variability in the signal range and in the data resolution. The segmentation process is robust, fast, and it provides fully automatically the femur and tibia bone with cartilage in a good accuracy.

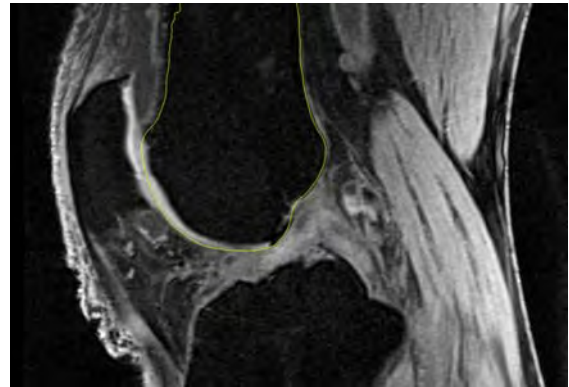


Figure 1: The yellow line shows the fully automatic segmentation of femur - bone with cartilage.

Acknowledgements

This project has been supported by the Forderstiftung Technopark Aargau, Forschungsfonds Aargau.

References

[Coots 2000] Coots T.: An Introduction to Active Shape Models. In Book "Image Processing and Analysis", Ed.R.Baldock and J.Graham,Oxford University Press, 2000, pp223-248.

LUMEN DETERMINATION IN PLAQUE-CONTAINING VESSELS

Marzia Buscema (1), Hans Deyhle (1), Anna Khimckenko (1), Georg Schulz (1), Thomas Pfohl (1), Simone E. Hieber (1), Christos Bikis (1), Simon Bugna (1), Andreas Zumbuehl (2), and Bert Müller (1)

1. Biomaterials Science Center, Department of Biomedical Engineering, University of Basel, Basel, Switzerland; 2. Department of Chemistry, University of Fribourg, Fribourg, Switzerland.

Introduction

Cardiovascular diseases are among the top causes of death worldwide [citation]. To prevent the high risk of mortality, shear-responsive liposomes [Holme, 2012] loaded with a vasodilator are proposed as an efficient treatment. Immune toxicity tests *in vitro* and *in vivo* have been performed [Bugna et al., 2016] as a prerequisite for developing nanopharmaceuticals. To understand the behavior of such promising phospholipid nano-containers under mechanical stimuli, small-angle X-ray scattering (SAXS) has been combined with microfluidics [Buscema, 2016]. Furthermore, micro computed tomography (μ CT) allows for three dimensional (3D) non-destructive imaging of the morphologies of healthy and calcified human coronary arteries.

Methods

Tomograms of a plaque-containing human coronary artery embedded in formalin were acquired in absorption contrast mode using the advanced laboratory system nanotom[®] m (GE, Wunstorf, Germany) equipped with a 180 kVp/15 W nanofocus tube. The scans were carried out at an acceleration voltage of 60 kV, a beam current of 310 μ A, a pixel size of 10.4 μ m, and 4.5 s exposure for each of the 1400 projections. Subsequently, the specimen was measured in grating-based phase contrast mode at the beamline P07 (DESY, Hamburg, Germany). The specimen was placed in a water tank to reduce phase-wrapping artefacts. The following parameters were used: 45 keV photon energy, 1.3 μ m pixel size, 900 off-axis projections over 360°, and 0.2 s exposure time per each phase step (four phase steps over one period of the interference pattern were taken at each projection angle). After embedding in paraffin, the calcified artery was measured at the P07 beamline again using the same setup and parameters described above.

Results

In order to optimize the shear-responsiveness of the liposomes, the lumen morphology of stenotic blood vessels has to be assessed. Herein, a calcified human coronary artery fixed in formalin was first visualized in absorption contrast mode with the

nanotom[®] m system. However, to allow the simultaneous visualization of the highly absorbing plaque and the soft tissue contained in the artery, the grating-based phase contrast modality was employed [Buscema, 2016]. Furthermore, the sample was embedded and measured in paraffin (Fig. 1, right) to evaluate the potential lumen deformation, which may occur during embedding for histology.

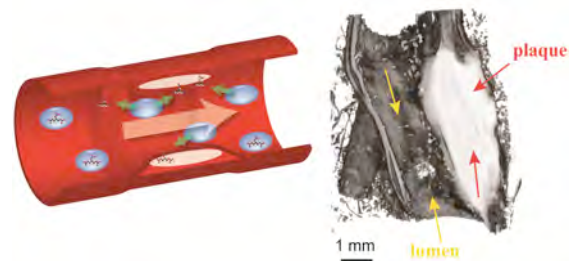


Figure 1: Sketch of plaque-containing blood vessel and shear-responsive liposomes loaded with nitroglycerin (left); 3D tomographic rendering of a paraffin embedded calcified human coronary artery acquired in absorption contrast mode (right).

Discussion

X-ray tomography-based imaging is a complementary tool to histology considered as the gold standard. The reconstructed dataset can be used for segmenting the artery lumen and are the grounds for flow simulations providing the average wall shear-stress range of healthy and constricted vessels [Holme, 2014].

Acknowledgements

The Swiss National Science Foundation (SNSF) via the NRP 62 “Smart Materials”, which funded this work partially, and the R’Equip project 133802 to acquire the nanotom are acknowledged.

References

- Bugna et al, Nanomedicine: NBM, 12:845-849, 2016.
- Buscema et al, Proc. SPIE, 9797:97970S-1, 2016.
- Holme et al, Nature Nanotechnol, 7:536-543, 2012.
- Holme et al, Nature Protocols, 9:1401-1415, 2014.
- Buscema et al, Proc. SPIE, 9967:99670O-1, 2016.

LABORATORY MICRO COMPUTED TOMOGRAPHY FOR THE VISUALIZATION OF THE MOUSE BRAIN

Christos Bikis (1), Philipp Janz (2), Georg Schulz (1), Gabriel Schweighauser (3), Jürgen Hench (3), Carola A. Haas (2), and Bert Müller (1)

1. Biomaterials Science Center, Department of Biomedical Engineering, University of Basel, CH; 2. Experimental Epilepsy Research, Department of Neurosurgery, University Medical Center Freiburg, DE; 3. Institute of Pathology, Department of Neuropathology, University Hospital Basel, CH;

Introduction

Micro computed tomography (micro-CT) using synchrotron radiation is a powerful method for the non-destructive visualization of biological specimens down to true micrometer resolution, capable of even revealing subcellular structures [Hieber, 2016]. Nevertheless, access to synchrotron radiation facilities is both limited and costly. We have thus proposed the use of a laboratory-based micro-CT system with an operation voltage of 40 to 60 kV for visualization of paraffin-embedded human cerebellum sample [Khimchenko, 2016]. Here, we show that the desktop system Skyscan 1275, that can operate reliably at an accelerating voltage of 20 kV, provides improved contrast. This allows for time-efficient visualization of the entire mouse brain.

Methods

Following extraction, the mouse brain was fixed in 4 % histological-grade buffered paraformaldehyde, dehydrated in ethanol, transferred to xylene, and finally embedded in a paraffin/plastic polymer mixture. Out of the obtained paraffin block, a cylindrical sample with a diameter of 8 mm was extracted by means of a robotic drill.

For the measurements, we have used the laboratory micro-CT system Bruker Skyscan 1275. For the measurements, an acceleration voltage of 20 kV and a beam current of 175 μ A were selected. The effective pixel size was set to 5.5 μ m. Over a range of 360°, 1200 projections were acquired equi-angularly. At each angular position, nine images with an exposure time of 0.6 s were acquired. This resulted in a total scanning time of two hours for a mouse brain hemisphere. After reconstruction with the manufacturer software, the resulting dataset was imported in the VGStudio MAX 2.1 software, for visualization and 3D rendering. This software was also used for the semi-automatic segmentation of brain structures of interest (e.g. hippocampus) by means of a region-growing approach.

Results

The beneficiary effect of micro-CT using photon energies below 20 keV for visualizing nervous tissue specimens embedded in paraffin is reflected in the quality of the acquired tomograms. Several anatomical structures of the mouse brain can be easily identified, such as the cerebral cortex, caudate putamen, corpus callosum, hippocampus, hypothalamus, and thalamus. In addition, both the ventricular system as well as several vessels are unequivocally localized (see selected images in Figure 1). The contrast of the acquired tomograms allows for the semi-automatic segmentation of specific brain structures of interest.

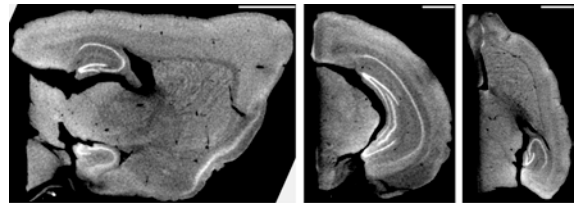


Figure 1: Sagittal, frontal and horizontal slices of the mouse brain. Scale bar: 1 mm.

Discussion

We have already reported the use of synchrotron-radiation double-grating interferometry for the investigation of the mouse brain [Bikis, 2016]. The Bruker 1275 micro-CT desktop system yields comparable image quality for the case of paraffin-embedded brain tissue, owing to photon energies below 20 keV and the paraffin embedding itself. Thanks to their ease of use, compact size and reasonable costs, such laboratory systems are an ideal candidate for complementing histology in several research and clinical applications.

References

- S. E. Hieber et al Scientific Reports 6:32156, 2016
- A. Khimchenko et al. NeuroImage 139:2636, 2016
- C. Bikis et al. Proceedings of SPIE 9967:996706, 2

IMAGING CELLULAR STRUCTURE OF HUMAN BRAIN TISSUE USING MICRO COMPUTED TOMOGRAPHY

Anna Khimchenko (1), Georg Schulz (1), Hans Deyhle (1), Christos Bikis (1), Simone E. Hieber (1), Natalia Chicherova (1,2), Gabriel Schweighauser (3), Jürgen Hench (3), Bert Müller (1)

1. Biomaterials Science Center, University of Basel, CH; 2. Medical Image Analysis Center, University of Basel, CH; 3. Institute of Pathology, Basel University Hospital, CH

Introduction

Currently, brain disorders account for about a third of the diseases in Europe [Olesen, 2003]. The progress in their diagnosis and treatment is partially hindered by the inability of suitable imaging modalities to provide cellular resolution in a label-free and non-destructive manner. Hard X-ray tomography is a powerful method to three-dimensionally investigate human tissues. The imaging in attenuation-contrast mode is often performed for hard tissues. The performance for low-density materials, however, is generally insufficient. Therefore, soft tissues are preferably visualized in phase-contrast modes [Lang, 2014] even down to subcellular level [Hieber, 2016]. Herein, the performance of laboratory-based micro computed tomography in absorption-contrast mode is compared to synchrotron radiation-based phase-contrast tomography and histology in the context of imaging the human cerebellum.

Materials and Methods

The human cerebellum was formalin-fixed, dehydrated and paraffin-embedded. The cylindrical specimen was 4 mm in diameter and 23 mm in height. Laboratory-based absorption-contrast micro computed tomography was carried out on the nanotom[®] m (GE Sensing & Inspection Technologies GmbH, Wunstorf, Germany). The tube acceleration voltage was set to 60 kV, the tube current to 310 μ A, the effective pixel size to 2.2 μ m and the exposure time to 2 s. Synchrotron radiation-based measurements were performed at Diamond-Manchester Imaging Branchline I13-2 (Diamond Light Source, Didcot, UK). The photon energy was set to 19 keV, for more details see [Khimchenko, 2016a]. Subsequent to the tomography measurements, the specimen was investigated by means of histology. For that, the specimen was re-embedded in a standard histological paraffin block, cut using a microtome, and stained with hematoxylin and eosin (H&E).

Results

Laboratory-based absorption-contrast tomography can provide an image contrast comparable to conventional histological sections [Khimchenko,

2016] and similar to a synchrotron radiation-based phase-contrast dataset [Khimchenko, 2016a] (Fig. 1). Analysing the Purkinje cells in the cerebellum, one can see that in the selected modalities a comparable number of morphological features can be identified.

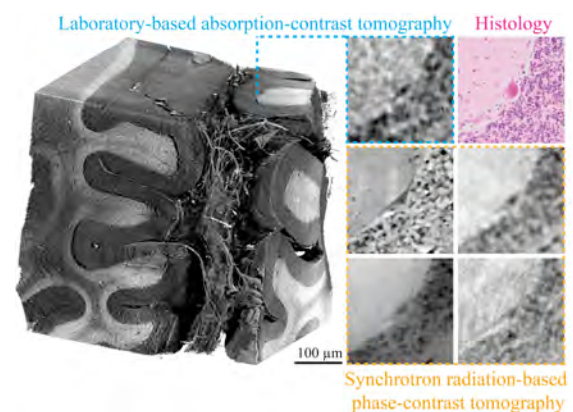


Figure 1: Comparison of laboratory-based micro computed tomography in the absorption-contrast mode to synchrotron radiation-based phase-contrast tomography and histology for visualizing individual neurons, on the example of the human cerebellum.

Conclusion

The results show the ability of laboratory-based absorption-contrast tomography to visualize individual cells and thus to become an important auxiliary modality in biomedical engineering.

Acknowledgements

The financial support of Swiss National Science Foundation projects 147172, 150164 and SNSF R'Equip project 133802 is acknowledged. The authors highly appreciated the assistance of the team of Diamond Synchrotron Radiation Facility, Didcot, UK.

References

- Hieber S. E. et al, Sci Rep, 6: 32156, 2016.
- Khimchenko A. et al, NeuroImage, 139: 26-36, 2016.
- Khimchenko A. et al, Proc SPIE, 9967: 996703, 2016a.
- Lang S. et al, J Appl Phys, 116: 154903, 2014.
- Olesen J. et al, Eur J Neurol, 10(5):471-7, 2003.

PHASE TOMOGRAPHY USING LABORATORY SOURCES TO VISUALISE CARTILAGE OF HUMAN KNEE

Georg Schulz (1), Anna Khimchenko (1), Griffin Rodgers (1), Christian Götz (1),
Magdalena Müller-Gerbl (2), Bert Müller (1)

1. *Biomaterials Science Center, Department of Biomedical Engineering, University of Basel, CH*; 2. *Musculoskeletal Research, Department of Biomedicine, University of Basel, CH*;

Introduction

For the three-dimensional (3D) visualization of hard tissues on the microscopic level X-ray micro-tomography (μ CT) using the conventional absorption contrast mode is the gold standard. With regards to lower density structures such as cartilage, however, this technique is suboptimal owing to the limited contrast. For brain tissues, for example, it was shown that synchrotron radiation-based phase tomography is the better choice [Schulz, 2010]. In order to overcome the restricted access our laboratory μ CT system has been equipped with a double-grating interferometer.

Materials and Methods

The knee of an 87-year-old female was fixed in 10 % formalin within 24 hours of death following the standard protocol at the Institute of Anatomy, University of Basel. For the X-ray phase tomography experiments a cylinder was extracted from the femur (see Fig. 1, left) near the contact area of the femorotibial joint, where a relatively thick cartilage layer was preserved.

The phase tomography was performed using a nanotom® m (GE Sensing & Inspection Technologies GmbH, Wunstorf, Germany) equipped with a double-grating interferometer (see Fig. 1, top), for more details see [Khimchenko, 2016]. Using the source mode 1 - corresponding to a source size of around 2 μ m - an acceleration voltage of 42 kV and a beam current of 310 μ A were adjusted in order to obtain a mean energy of 30 keV, which is the design energy of the interferometric setup. For the phase retrieval, 11 phase steps over two periods of the interference pattern with an exposure time of 9 s were acquired at each angular position. For tomographic reconstruction 400 radiographs were recorded over an angular range of 360°. Phase recovery and reconstruction of the data were done in Matlab R2014a (MathWorks, Natick, USA).

Results

The performance of the setup was verified by visualizing a femoral cylinder fixed in formalin containing bone and cartilage. Figure 1 right shows a false colour 3D rendering of the specimen. Using

an intensity-based segmentation three structures, i.e. bone (yellow), cartilage (blue) and formalin solution (cyan) can be identified. A thickness of the cartilage of around 3.4 mm was found.

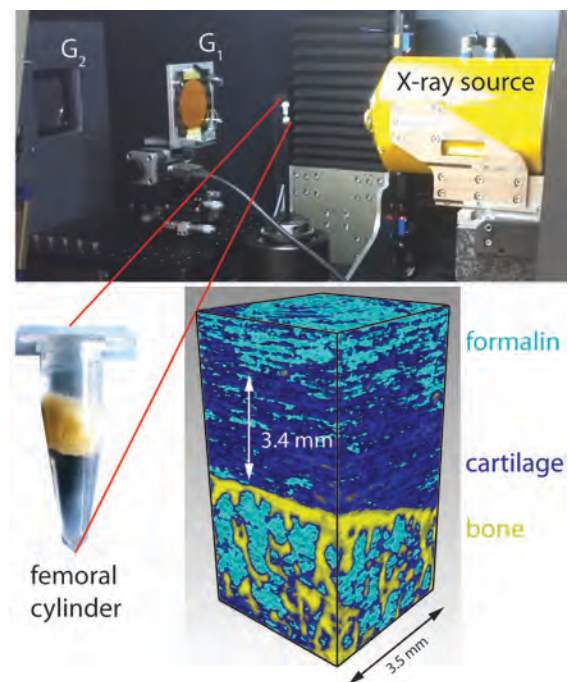


Figure 1: X-ray phase tomography of a human femoral cylinder (left) using a laboratory-based grating interferometry setup (top). The 3D rendering (right) shows an intensity based segmentation of bone, cartilage and formalin.

Conclusion

The lab-based phase tomography results using a grating interferometer of a human femoral cylinder show promising results for further investigations of cartilage without the use of any contrast agent.

Acknowledgements

The authors acknowledge the financial support of Swiss National Science Foundation projects 147172, 150164 and SNSF R'Equip project 133802.

References

- Schulz G. et al., J R Soc Interface, 7: 1665-1676, 2010.
- Khimchenko A. et al., Proc SPIE, 9967: 996703, 2016.

PRECISION MEASUREMENTS OF ORAL SCANNERS

Christoph Vögtlin (1), Kurt Jäger (1), Georg Schulz (1), Bert Müller (1)

1. Biomaterials Science Center, Department of Biomedical Engineering,
University of Basel, CH;

Introduction

The preparation of prosthetic restorations and orthodontic appliances requires three-dimensional data on the patient's dentition. The disadvantages of the approach include the unfavorable flavor of the impression materials and the human choke impulse. In order to overcome these discomforts, dentists currently employ scanners that provide digital impressions of the patient's dentition. With these digital data, the dentist can simplify workflow and reduce costs. Many dentists, however, are afraid that the accuracy of the present oral scanners does not reach the precision of the replicas obtained using the well-established, conventional protocol. The precision of iTero™ Intraoral Scanner (Straumann Holding AG, Basel, Switzerland) and LAVA™ Chairsides Oral Scanner (3M™ ESPE™ AG, Rueschlikon, Switzerland) were analysed by comparing micro computed tomography (micro-CT) scans of master models with a steel reference using non-rigid registration algorithms [Vögtlin, 2016].

Materials and Methods

In this study, we investigate the accuracy of the intraoral scanner "True Definition Scanner" (3M Espe, Seefeld, Germany) taking advantage of high-resolution micro-CT using the tomography system nanotom® m (GE Sensing & Inspection Technologies, Wunstorf, Germany). For this purpose, we produced five reference models with constant transversal dimension. We have considered five situations in the front region, which were scanned three times each with the intraoral scanner. The reference models were imaged using the micro-CT system. The micro-CT measurements were taken with an acceleration voltage of 120 kV, a beam current of 100 μ A, and a pixel length of 30 μ m. Using an in-house script (MATLAB R2015b, Mathworks, Natick, USA), distances between reference points (defined as the center points of the hollow cylinders at specified heights, see Fig. 1) were determined from micro-CT data and intraoral scans.

Results

The distances between the four reference points in the intraoral scans were compared to the distances measured in the micro-CT data. The sagittal distance in the intraoral scans had a precision on the

micrometer level and the transversal distances a precision of tens of micrometers.

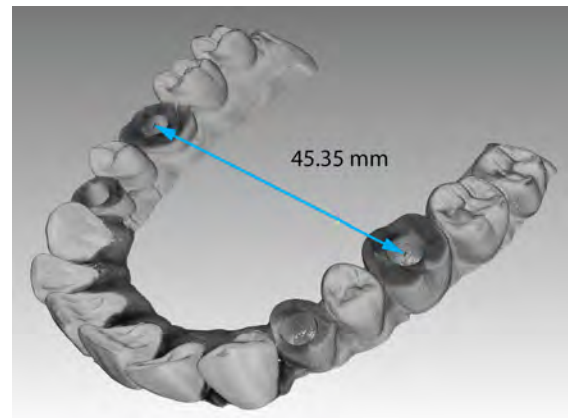


Figure 1: 3D rendering of microtomography data showing the distance between two reference points.

Conclusion

The precision of intraoral scanners can be investigated by laboratory-based X-ray micro-CT. The present study elucidates that the intraoral scans using the "True Definition Scanner" are clinically sufficient.

Acknowledgements

The authors acknowledge the financial support of Swiss National Science Foundation R'Equip project 133802. The study originated in the framework of a master thesis at Danube Private University (Krems, Austria).

References

Vögtlin G. et al., Phys Med, 1: 20-26, 2016.

MULTI-CENTER ABDOMINAL CT PROTOCOLS: A PHANTOM STUDY ON IMAGE QUALITY AND RADIATION DOSE LEVELS.

Damien Racine (1), Nick Ryckx (1), Francis R. Verdun (1)

1. Institute of Radiation Physics – Lausanne University Hospital, Rue du Grand-Pré 1 – 1007 Lausanne – Switzerland

Introduction:

(1) To highlight the spread of patient exposure and image quality performances for various abdominal protocols. (2) To ensure that radiation dose reductions in abdominal CT protocols do not impair the detection of low-contrast structures.

Methods:

An anthropomorphic abdominal phantom (QRM, Moehrendorf, Germany) with two optional rings (2.5 cm and 5 cm), representing the attenuation of an adult abdomen of 50 kg (small phantom), 75 kg (medium phantom) and 100 kg (large phantom), was scanned on 70 CT machines in the Western part of Switzerland. The phantom contains in the axial plane four spheres of 5, 6 and 8 mm in diameter with a contrast of 20 HU relative to the background at 120 kV. For statistical reasons, each phantom size was systematically scanned 10 times using local clinical settings of the portal phase for the detection of focal liver lesions (FLL); 40 regions of interest (ROIs) including the target and 150 ROIs with background noise only were extracted. Low contrast detectability (LCD) was objectively assessed using a Channelized Hotelling mathematical model Observer (CHO) with ten dense differences of Gaussian channels for the calculation of a receiver operating characteristic (ROC) curve. For each lesion size, the area under the ROC curve (AUC) was used as a figure of merit (FOM). A new image quality metric, called the weighted AUC (AUC_w), was proposed to combine the AUC results of all 3 different lesion sizes in a single metric. The displayed CTDI_{vol} was used as a radiation dose metric.

Results:

The median dose used for acquisitions is equal to 5.8 mGy, 10.5 mGy and 16.3 mGy, respectively for the small, medium and large phantoms. For the small phantom, the median image quality is equal to 0.977 with an interquartile range (IQR) equal to 0.027. For the medium phantom the dispersion increased and the median image quality decreased (AUC_w = 0.926 and IQR = 0.05). For the large phantom, despite a large range of CTDI_{vol}, the

median image quality also decreased (AUC_w = 0.89 and IQR = 0.068) and six centers appeared as outliers with relatively limited AUC_w scores (AUC_w inferior to 0.75), due to very low CTDI_{vol} values.

Conclusions:

The use of a CHO model showed that the majority of institutions performed reasonably well when searching FLL. However, for some outliers, the CTDI_{vol} values were so small that image quality outcomes were clearly not adequate for the intended task. Moreover, the spread of image quality levels was associated with a large CTDI_{vol} distribution, showing that the concept of diagnostic reference levels should be revisited to take into account the image quality aspect. This would ensure comparable diagnostic performance image information content whatever the type of CT unit.

Multi-modality Sensory Feedback System for Upper Limb Amputees

Huaiqi Huang^(1,2), Tao Li⁽¹⁾, Christian Enz⁽²⁾, Claudio Bruschini⁽²⁾, Christian Antfolk⁽³⁾, Jörn Justiz⁽¹⁾, and Volker M. Koch⁽¹⁾

1. Institute for Human Centered Engineering (HUCE), Bern University of Applied Sciences, Switzerland;
2. Integrated Circuits Laboratory, EPFL, Switzerland
3. Department of Biomedical Engineering, Lund University, Lund, Sweden

Introduction

There are an estimated 3 million upper limb amputees all over the world. Myoelectric prostheses provide the most dexterous control among all the available commercial prostheses. However, this type of prostheses faces a high rejection rate because they do not provide sensory feedback. Providing sensory feedback can not only increase the functionality of prosthesis, but can also introduce a feeling of embodiment.

System Description

The sensory feedback system consists of five sensor modules embedded on a robotic hand, Bluetooth low energy (BLE) communication modules, and a multi-modality haptic display (Fig. 1).

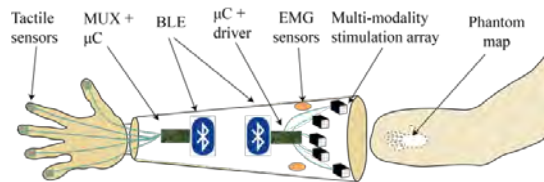


Fig. 1 Block diagram of the sensory feedback system

The tactile sensors used in the system are piezoelectric barometric sensors. The sensor PCB was covered with a 5 mm silicone coating for measurement and protection. The sensory data was communicated through a Bluetooth low energy module (CC2640R2F, Texas Instrument). The multi-modality stimulation device combining vibrotactile and mechanotactile (Fig. 2 (a)) was integrated in a 3D-printed casing (Fig. 2 (b)).

Experimental Setup and Results

Three amputees (A1, A2, and A3) participated in three experiments: 1) Localization, 2) Stimulation intensity identification, and 3) Simultaneous localization and intensity identification. The results

indicate that the multi-modality stimulation device helps to improve both localization and intensity identification performance (Fig. 3).

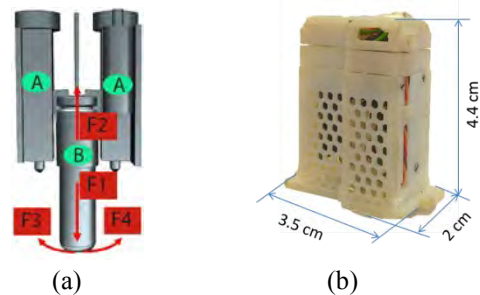


Fig. 2 Custom-designed multi-modality stimulation device. (a) The design concept of the device. Two servo motors (A) are used to push down a cylindrical vibrator (B). (b) The device integrated in a 3D printed casing.

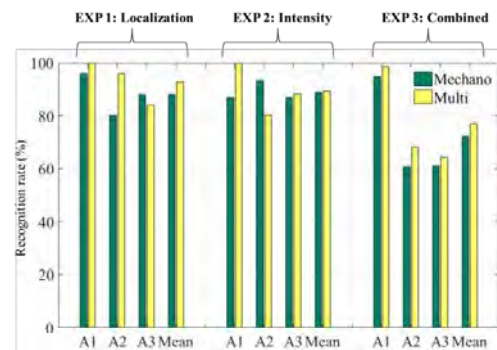


Fig. 3 The recognition rate of three amputees (A1, A2, and A3) and the averaged recognition rate during three sub-experiments. The green and yellow bars represent the recognition rate of mechanotactile and vibrotactile stimulation, respectively.

Conclusion

To the best of our knowledge, this is the first complete non-invasive sensory feedback system combining mechanotactile and vibrotactile stimulation. The multi-modality feedback system proves to be more effective than the single modality.

A WEARABLE SYSTEM FOR MULTICHANNEL BIOIMPEDANCE AND MULTILEAD ECG MONITORING

Michael Rapin (1, 2), Fabian Braun (1, 3), Josias Wacker (1) and Olivier Chételat (1)

1. CSEM SA, Switzerland; 2. ETHZ, D-HEST, Switzerland; 3. EPFL, LTS5, Switzerland

Introduction

Cooperative sensors (CS) are a novel measurement architecture for acquiring biosignals based on active electrodes. In contrast to traditional approaches, CS do neither require shielded or complex multi-conductor cables, nor a central electronic unit. This advantage significantly simplifies their connection and integration in a garment. We have previously shown ambulatory ECG measurement with CS [Rapin, 2017]. Here, we show how a wearable CS system is used to simultaneously measure multichannel bioimpedance (IMP) and multilead ECG signals.

Methods

Fig. 1 shows the CS architecture with three different types of sensors: 1) the master sensor, 2) type I sensors for IMP current injections and 3) type V sensors for measuring voltages. All sensors are linked together with two unshielded wires. The ref. wire sets the reference potential for all sensors. Voltages (v_1 to v_{n-1}) are amplified, filtered and digitized onsite by the electronic embedded in type V sensor which simultaneously measure the ECG (0.05 to 150 Hz) and IMP signals resulting from the IMP current injections (~ 50 kHz).

The com. wire is used for communication between the CS. Communication from the master sensor to the other sensors is performed via voltage impulses (~ 2 MHz) sent by u_{sync} and received as u_1 to u_n . Moreover, the current sources i_1 to i_{n-1} allow the type V sensors to communicate with the master sensor to transfer the digitized signals. Data are sent as current impulses and are read as i_{com} .

Fig. 2 shows an example of integration of the wearable monitoring system based on CS. The vest includes the master sensor (black), 12 type V (orange) and 12 type I (grey) sensors. In the present configuration of the system, 144 impedance channels are measured at a rate of 80 frames per

second. This system was tested on one healthy male subject. Fig. 3 shows a set of IMP signals measured during normal breathing (4 first cycles) and deep breathing (4 last cycles).

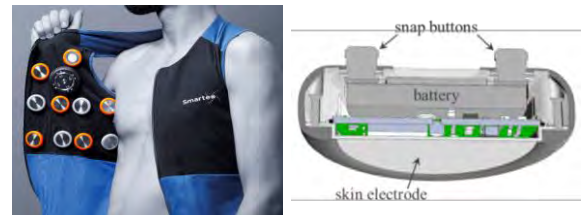


Figure 2: Wearable sensors integrated in a vest (left) and example of integration of a CS (right).

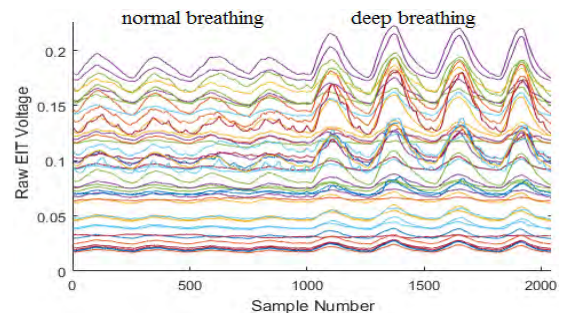


Figure 3: Bioimpedance signals measured with CS.

Discussion

This paper shows a novel sensor architecture for ambulatory multichannel IMP and multilead ECG signals monitoring. The presented system is fully wearable thanks to the CS technology, which allows linking the sensors together with only two unshielded wires and does not require any central electronic unit. Such a system is able to measure data allowing for electrical impedance tomography (EIT) [Adler, 2009], paving the way toward a new generation of wearable EIT systems.

References

- Adler et al., *Physiol. Meas.*, 30.6:S35, 2009.
- Rapin et al., *IEEE TBME*, in press, 2017.

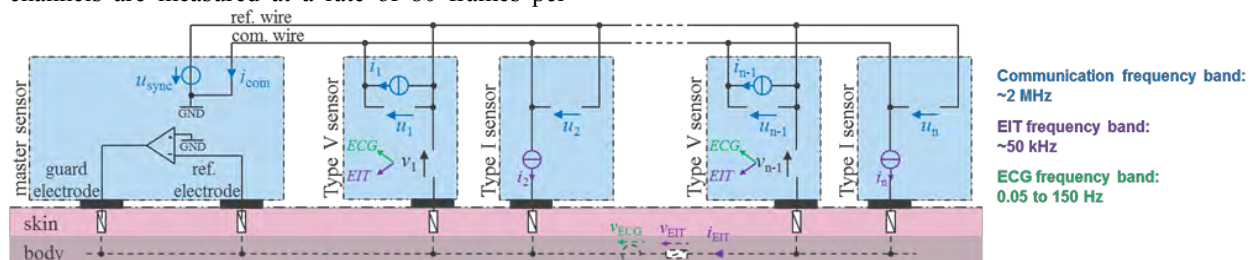


Figure 1: Architecture of the wearable monitoring system based on CS.

MANIPULATION OF SINGLE NEURONS AND DEFINED NEURAL CIRCUITS WITH FORCE-CONTROLLED NANOPIPETTE

Ines Lüchtfeld (1), Mathias J. Aebersold (1), Vincent Martinez (1), Harald Dermutz (1), László Demkó (1), Tomaso Zambelli (1), Janos Vörös (1)

1. Laboratory of Biosensors and Bioelectronics, Institute for Biomedical Engineering, ETH Zurich, Zurich CH-8092, Switzerland

Introduction

In conventional biology, the average of many cells in a tissue sample or culture is used for investigations. However, the assumption of homogeneity within the multitude of cells might lead to false conclusions, giving rise to the need for single cell investigations. Especially the field of neuroscience would profit immensely from understanding how individual neurons behave and communicate in small networks in order to unravel how the billions of nerve cells in the brain work together to perform its basic functions.

Consequentially, the investigation of neurons on a single cell level and in small engineered networks requires specialized tools that provide a chemical, electrical and mechanical interface between the cell and its environment.

Methods

Here, we present the FluidFM as such a versatile interface with precise temporal and spatial control. The FluidFM system is based on an atomic force microscopy cantilever with an embedded microchannel that ends in an aperture with sizes down to 300nm. It thus functions as a force-controlled nanopipette for diverse applications.

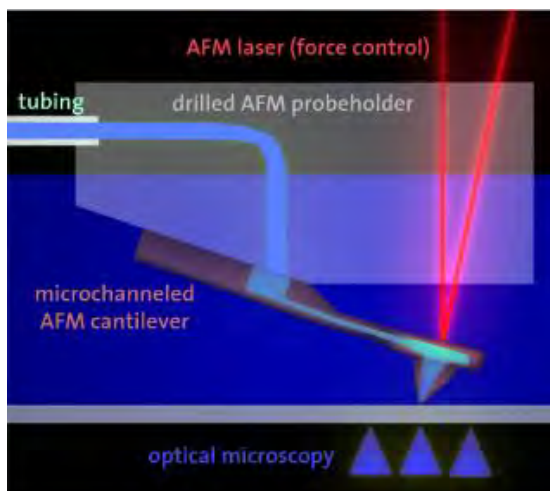


Figure 1: Schematic of the FluidFM technology.

Results

Recently, we achieved the spatially controlled patterning of single neurons by using highly flexible SU-8 cantilevers to individually place cells onto adhesive surfaces [Martinez, 2016]. Additionally, the FluidFM system was used to create defined patterns of the cell-adhesive poly-L-lysine on a non-fouling PLL-g-PEG background [Dermutz, 2014]. This technique enables control over neuron adhesion and neurite guidance. Furthermore, external chemical stimulation of subcellular sections of single neurons is possible by localized release of the neurotransmitter glutamate from the FluidFM tip, acting as an artificial synapse.

Discussion

The combination of these techniques opens up the potential to investigate the behaviour and function of small neural networks with a new level of control [Aebersold, 2016]. In addition, this technique is ideally suited to address the multitude of open scientific questions in the upcoming field of single cell biology.

References

- Aebersold, M.J. et al, TrAC Trends Anal. Chem., 78: 60-69, 2016.
- Dermutz, H. et al, Langmuir, 30.23: 7037-7046, 2014.
- Martinez, V. et al, Lab Chip, 16.9:1663-1674, 2016.

FLUID FM: A PLATFORM FOR 3D ADDITIVE MANUFACTURING OF METAL STRUCTURES AT THE MICRON SCALE

Cathelijn A J van Nisselroy (1), Luca D Hirt (1), Alain S Reiser (2), Ralph Spolenak (2), János Vörös (1), Tomaso Zambelli (1)

1. Laboratory of Biosensors and Bioelectronics, Institute for Biomedical Engineering, ETH Zurich, Switzerland; 2. Laboratory of Nanometallurgy, ETH Zurich, Switzerland

Introduction

Fabrication of tailored metal patterns and structures has been a topic of growing interest in the last decade [Skylar-Scott, 2016]. Where traditional fabrication methods are often limited to 2D arrangements, additive manufacturing (AM) allows for the fabrication of structures without geometrical constraints [Hirt, 2017]. Here we report the use of the Fluid Force Microscope (FluidFM), as an AM technique for voxel by voxel printing of copper (Cu) structures with sub-micron resolution.

Methods

Printing of the Cu structures is achieved via local electroplating under the apex of the FluidFM's hollow cantilever. This is accomplished in an electrochemical cell, consisting of the electrolyte (H_2SO_4) and a 3-electrode set-up. Close to the electrode cell's gold surface, the metal salt solution ($CuSO_4$) is ejected from the cantilever and reduced under the tip by application of an overpotential. When the growing voxel touches the tip, it deflects the cantilever, as shown in Figure 1. This serves as a feedback signal for the system, resulting in tip retraction and movement of the cantilever to the next printing position.

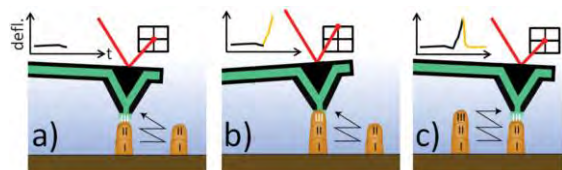


Figure 1: FluidFM's automated printing principle. (a) Voxel growth underneath the tip, (b) The growing voxel touches the tip and deflects the cantilever, (c) The system responds by retracting the cantilever and moves on to the next spot.

Results

We have printed a variety of Cu geometries (Fig. 2 a-e) with sub-micron resolution. By changing deposition time and pressure, the size of each structure could be tailored (Fig. 2a).

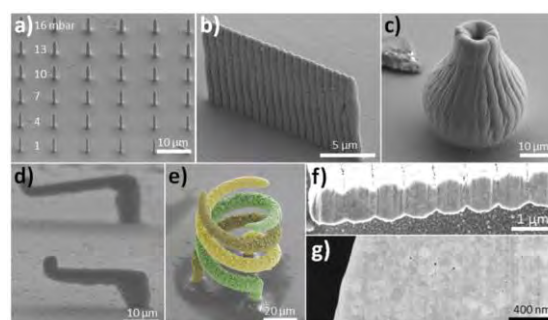


Figure 2: SEM pictures of printed Cu Structures. (a) Influence of deposition time and pressure on pillar formation, (b) Wall of pillars, (c) Vase (d) Overhanging structures, (e) Intertwined helices, (f-g) FIB cross sections of printed structures.

Additionally, focused ion beam (FIB) cross sections revealed a dense microstructure of the printed structures (Fig. 2 f-g). To verify the material purity, the structures were subjected to energy-dispersive X-ray spectroscopy (EDX), showing no contaminations.

Discussion

The major advantages of this technology are the automated fabrication, material purity, sub-micron resolution and 3D configuration. However, the printing speed and surface roughness are points of improvement. Currently, the printing of different metals is being studied, as well as the possibility to do multi-material printing. Other applications of this technique could, for instance, be the 3D printing of cells, micropatterns or (conductive) polymers.

Acknowledgements

This project was supported by the Commission for Technology and Innovation (KTI-CTI).

References

Skylar-Scott et al, PNAS, 113:6137-6142, 2016.
Hirt et al, Adv. Mater, 29:1604211, 2017.

SIDEWAY-FABRICATED SU-8 HOLLOW CANTILEVERS AND APPLICATIONS

Hana Han(1), Vincent Martinez(1), Mathias Aebbersold(1), Tomaso Zambelli(1), Janos Vörös(1)

1. Laboratory of Biosensors and Bioelectronics, Institute for Biomedical Engineering, ETH Zurich, Switzerland

Introduction

Most of the applications with microchanneled AFM cantilever require a tip. Apertures of the standard cantilevers based on silicon technology were fabricated by milling via tedious FIB or corner photolithography which only provides the pyramidal tip geometry [Berenschot, 2012]. Here we present the novel approach to obtain a hollow tip on every cantilever without further processing after photolithography

Methods

The hollow SU-8 cantilever with aperture has been fabricated with sideway as shown in Fig.1. All the parameters were adjusted to present work based on the previous fabrication process [Martinez, 2016].

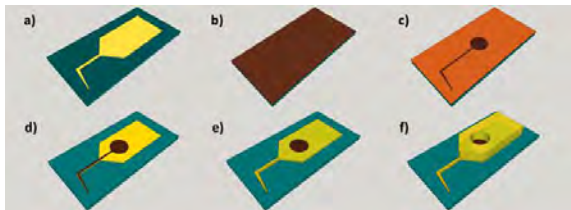


Figure 1: Sideway microfabrication process for SU-8 micropipette. a) Patterning of 1st SU-8 layer, b) Deposition of Cu as a seed layer, c) Patterning of photoresist and Cu electroplating, d) Strip off the photoresist and Cu seed layer, e) Patterning of the 2nd SU-8 layer, f) Patterning of the SU-8 chip layer

For the functionality test, each device was released from the wafer and glued on the customized plastic clip to be simply fixed to the AFM probe holder.

Results

We have fabricated the hollow AFM cantilevers made entirely of SU-8 having a hundred-microns long tip. The length of cantilever arm and tip could be designed dependently for different types of cantilever (Fig. 2a-b). Apertures of the all types of cantilever had a rectangular shape, in a range of 8-15 μm by 10 μm .

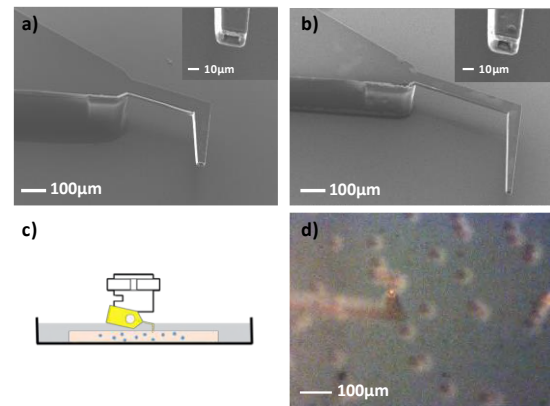


Figure 2: a,b) SEM images of sideway fabricated cantilevers and its apertures, c) Schematic of bead manipulation in 3D gel experiment and d) optical view

To confirm their functionality, cantilevers were used to pick up microbeads embedded in hydrogel (Fig. 2c). An optically selected bead was sucked against the aperture edge by applying a negative pressure. Then, the cantilevers were gradually retracted until the bead completely emerged from the gel (Fig. 2d).

Discussion

The sideway fabrication process indeed opens several opportunities for different tip shapes and lengths instead of a single pyramidal geometry, inside a single wafer. The size and shape of the apertures were restrained to rectangle and lowest 2.5 μm which has a limitation in nanometer-scale applications.

Acknowledgements

This work is supported by Swiss Nation Science Foundation.

References

Berenschot et al, Small, 8: 3823–3831, 2012.
Martinez et al, J Micromech. Microeng, 26:1-10, 2016.

REAL-TIME MEASUREMENT OF GLUCOSE CONCENTRATION IN 3D CULTURE OF HUMAN INTERVERTEBRAL DISC CELLS

Daniela A Frauchiger (1), Rahel D May (1), Lorin M Benneker (2), Andreas K Koch (3), Benjamin Gantenbein (1)

1. Institute for Surgical Technology and Biomechanics, University of Bern, Bern, Switzerland;
2. Department of Orthopaedic Surgery, Inselspital, Bern University Hospital, University of Bern, Switzerland; 3. C-CIT Sensors AG, Wädenswil, Switzerland

Introduction

Glucose uptake is a crucial task for all cells. However, intervertebral disc (IVD) cells depend solely on passive diffusion of glucose and hence measurement of glucose concentration is considered being of special importance [Grunhagen, 2011; Huang, 2014]. Also, as the main transportation roads might get blocked in disc degeneration or by ageing. Here, we hypothesized that due to the location of the different tissues, i.e. the nucleus pulposus cells (NPC) in the center of the disc, the annulus fibrosus cells (AFC) and the cartilaginous endplate cells (EPC) glucose consumption rate differs. We assume that consumption is the highest with cells being in the proximity of blood vessels i.e. EPC and that the cells in the center (NPC) would require the lowest glucose consumption rate. In this project, we tested our hypothesis by using primary IVD cells in 3D culture from trauma patients and measuring glucose concentration in the media in real-time with a novel sensor.

Methods

Primary human AFC, NPC and EPC were isolated using a mild two-step digestion protocol consisting of pronase and collagenase type 2 with written consent of patients. Subsequently, cells were expanded in 2D and were resuspended at passage 2 in 1.2% alginate at a density of 4 Mio cells/ml and beads were formed using a syringe pump (1.8 ml/min, 22G). 30 beads were added per T-25 culture flask that was equipped with a glucose sensor (C-CIT Sensors AG, Switzerland) and cultured in 9 ml hyperglycaemic medium (DMEM supplemented with 4.5g/l glucose and 10% FCS) under agitation (10rpm), see Figure 1A. Glucose concentration, proportional to current in nA, was recorded over seven days and media was replaced after 3-4 days. Additionally, cell activity (resazurin red assay), DNA and glycosaminoglycan (GAG) content were determined on day 1 and on day 7.

Results

Real-time glucose monitoring *in vitro* was successful, Figure 1B. For the glucose consumption, linear regression of current (nA) was performed.

Slopes of least-square fitted linear regression were used for comparison among cell types. Prior media change, all cell types showed a similar glucose consumption rate. After media change, however, EPC presented a higher glucose consumption than AFC and NPC, Figure 1C.

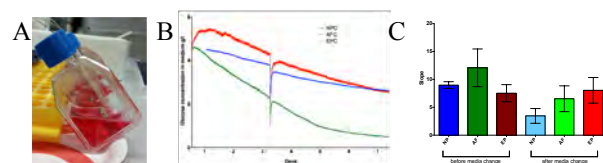


Figure 1: A Glucose consumption monitored in real-time for human AFC, NPC and EPC. B Slopes of current before and after media change of 5 experiments \pm SD.

Discussion

It seems there is a difference in glucose consumption between the different cell types of the IVD. Especially, the glucose consumption behaviour after media change could be explained by their location close to the nutrient transport route, i.e. the capillary system of the vertebrae respectively away from such routes. So, they should be adapted to higher glucose levels than cells in the centre of the disc, which rely on pure diffusion. In the near future, we plan to repeat this experiment and to vary glucose concentration to determine the ideal glucose range for cell culture and to investigate possible IVD treatment approaches.

Acknowledgements

This project was supported by the Gebert R uf Foundation project # GRS-X028/13. We thank Stefan Spichiger and Ferdi Cagayan from C-CIT Sensors AG. Further, we thank Eva Roth for assistance with IVD cell isolation.

References

Grunhagen T et al, Orthop Clin North Am, 42(4):465-77, 2011.
Huang YC et al, Nat Rev Rheumatol, 10(9):561-6, 2014.

THREE-DIMENSIONAL MAGNETIC CAMERA FOR BIOMEDICAL APPLICATIONS

Joris Pascal (1), Felix Yeung (1), Sven Knecht (2)

1. University of Applied Sciences and Arts Northwestern Switzerland, Muttenz, Switzerland;
2. University Hospital Basel, Switzerland

Magnetic camera concept and applications

We present a three-dimensional magnetic camera consisting in an array of multiple CMOS integrated monolithic three-dimensional Hall effect sensors [Pascal 2008]. Based on its modular concept, the camera can cover different volumes and performs sampling up to 3000 samples per second of the three-dimensional magnetic flux density signals. The magnetic camera has been applied for the characterization of magnetic manipulation instrumentation systems for electrophysiology procedures. Besides, thanks to the large dynamic range of the Hall effect sensors, we were able to measure experimentally the magnetic field gradient map within a clinical MRI. The new magnetic camera described in this paper has to our knowledge no commercial equivalent. It answers to the need of experimental characterization of e.g. magnetic manipulation systems and MRI and offers the designers some new experimental performance assessment capabilities. The camera is either suited for small object manipulation where the steering field reaches a magnitude of about 1 mT or for electrophysiology applications where the magnetic steering of catheters requires a magnetic flux density of typically 100 mT. Measurement of larger magnetic fields has been demonstrated within a three Tesla MRI.

Experimental results

Figure 1 shows the superimposition of the photograph of the Stereotaxis Niobe® magnetic navigation system with the vector map acquired with our magnetic camera at the University Hospital Basel (Switzerland). This mapping allows one to identify the homogeneous region where the catheter magnetic control is optimal. It also represents the magnetic field gradient that settles between the two magnets. Figure 2 depicts the dynamic magnetic field measurement performed within a three Tesla MRI at University Hospital Nancy (France) during a MRI gradient sequence. This measurement illustrates the magnetic resolution of our sensor system that is able to measure milli-Tesla changes within a three Tesla static field.

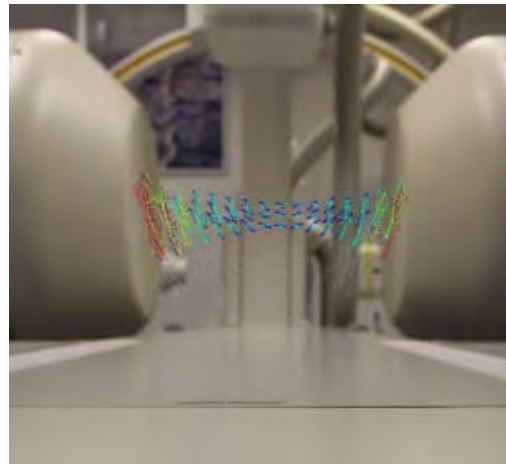


Figure 1: 3D map of the magnetic field generated by the Stereotaxis Niobe® magnetic navigation system. 100 mT is measured at the centre whereas the magnetic field at the magnet surface reaches 700 mT.

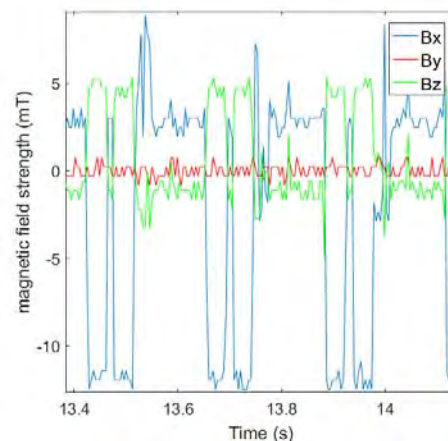


Figure 2: Magnetic field gradients measured within a three Tesla clinical MRI. The measurement is shown for one single three-dimensional Hall sensor located within the MRI tunnel.

References

- Pascal, Joris, et al. "First vertical Hall device in standard 0.35 μm CMOS technology." *Sensors and Actuators A: Physical* 147.1 (2008): 41-46.

A WIRELESS SENSOR FOR MEASUREMENT OF SOFT TISSUE STRAINS IN VIVO

Qiang Zhang (1), Flurin Stauffer (2), William R. Taylor (1), Klas Tybrandt (2), Roland Küng (3), Janos Vörös (2)

1 Laboratory for Movement Biomechanics, ETH Zürich, Switzerland

2 Laboratory of Biosensors and Bioelectronics, ETH Zürich, Switzerland

3 Center for Communications Engineering, Zürich University of Applied Sciences, Switzerland

Introduction

Ligaments and tendons suffer from a high incidence of injury [Dick, 2007], and often require subsequent reconstruction surgery and rehabilitation [Escamilla, 2012]. The associated financial costs and long-term impairments on each patient's movement ability highlight the needs for an improved understanding of the functional demands on the soft tissues surrounding the joint. Ligament injury is widely considered to be associated with excessive strains [Hosseini Nasab, 2016], but access to soft tissue loading conditions in vivo remains limited. Here, a number of different methods have been utilized [Fleming, 2003, Park, 2015]. However, while traditional strain sensors offer a feasible and accurate tool for strain assessment, they are limited in their requirement for continuous wires that cross the skin and thus limit their ability to monitor soft tissue strain patterns during healing progression. The design of a new wireless strain sensor is therefore warranted.

Recently, significant progress has been made towards stretchable electronics that use conductive elastomers such as nanowires [Amjadi, 2016, Tybrandt, 2016]. Combined with advanced RFID technology, such approaches might allow for implantable and wearable applications that are able to wirelessly transmit across the skin, and therefore open perspectives for diagnosis, monitoring, and therapeutic purposes in medicine. The aim of this study was therefore to establish whether such approaches could be tailored to provide accurate strain data and validate the performance of such a sensor under preliminary stretching tests.

Methods

We employed a fast prototyping fabrication method that used a wax printer for filtration patterning of metallic nanowires on a PVDF membrane [Tybrandt and Voros, 2016]. The layers were transferred onto silicone rubber for multilayer structures to create a stretchable capacitor. To complete the LCR resonant circuit, a coil inductor was bonded to the capacitor using conductive epoxy, and encapsulated using a silicone sealant. The sensor allowed wirelessly data transmission through electromagnetic coupling by a readout coil and a portable Arduino-based network analyser.

A tensile testing machine (DO-FB0.5TS, Zwick/Roell) was employed to stretch the sensor in 0 to 50% strain cycles at 0.5% strain per second. The resonance frequency of the sensor was recorded continuously during the stretching test.

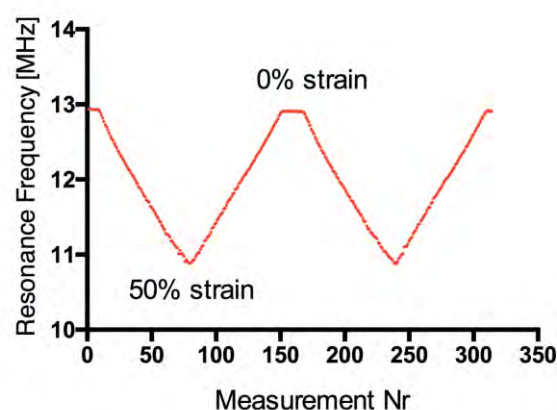


Figure 1. Change of resonance frequency during stretching from 0 to 50% strain.

Result & Discussion

The change of resonance frequency varied inversely and nearly linearly with respect to the strain, with the frequency decreasing from 12.9 MHz at 0% strain to 10.9 MHz at 50% strain (Fig. 1). Using novel micro-fabrication methods for simple and fast prototyping, we have successfully designed a passive and wireless strain sensor using a highly stretchable electronic resonance circuit that could be readout wirelessly using electromagnetic coupling by a portable device. The sensor element changed its resonance frequency linearly with strain and remained conductive throughout, including strains of up to 50% (over two times of the ultimate strain of human ligament). As a next step, the strain sensor will be validated in vitro on a bone-ligament-bone sample, towards in-vivo application.

References

- Amjadi M., et al., *Ad. Func Mat*, 26: 1678-1698, 2016.
- Dick R., et al., *J Athl Train*, 42: 194-201, 2007.
- Escamilla, et al., *J Or Sp Phys Ther*, 42: 208-220, 2012.
- Fleming B. C., et al., *AJSM*, 31: 701-707, 2003.
- Hosseini Nasab, et al., *PLoS One*, 11: e0167106, 2016.
- Park K. K., et al., *J Biomech*, 48: 418-424, 2015.
- Tybrandt K., et al., *Small*, 12: 180-184, 2016.

INCUBATOR TEMPERATURE CALIBRATION AND MONITORING FOR HYPERTHERMIA IN-VITRO EXPERIMENTS

Mathias S. Weyland (1), Dietmar Marder (2), Katarzyna J. Nytko (3), Stephan Scheidegger (1,2)

1. ZHAW School of Engineering, Zurich University of Applied Sciences Winterthur, Switzerland; 2. Radioonkologie-Zentrum KSA-KSB Aarau, Switzerland; 3. Division of Radiation Oncology, Vetsuisse Faculty University of Zurich, Zurich, Switzerland

Introduction

Incubators such as the Sanyo MCO-18AC are used in in-vitro experiments to simulate hyperthermia treatment of cells. It is critical for those devices to maintain a stable and accurate temperature, as even small variations in temperature are known to affect the underlying biochemical processes [Sapareto, 1984]. We present a system to monitor the temperature on the inside of incubators with high accuracy, low cost and in a live and scalable manner.

Methods

The system consists of three parts: A computer, a hardware interface and sensor heads. The computer is running a program that displays a temperature graph in real time and stores the acquisitions in a text file for later processing. On start-up, the program detects all sensor heads, enumerates them and retrieves the calibration coefficients that have been programmed into the sensor during manufacture. The interface connects to the computer via USB and connects to the sensor heads via a 5 m long ribbon cable. The microcontroller installed on the board is programmed to poll each sensor head at a frequency of 5 Hz via SPI and to send the raw readout to the computer. There, the readout is converted to a temperature using the calibration coefficients retrieved initially. Each sensor head consists of a custom board which carries a TE Connectivity TSYS01 Digital Temperature Sensor and supportive circuitry to achieve an accuracy of ± 0.1 °C and a resolution of 0.01 °C. The board is coated with PLASTIK 70 conformal coating by CRC Industries to withstand liquids and the harsh environment inside the incubator.

The system was calibrated in a Cole-Parmer Polystat heating circulating bath against a TP-200 reference probe of ± 0.3 °C accuracy and 0.1 °C resolution, and a mercury thermometer of 0.1 °C resolution. Calibration was performed at the set points of 37, 41, 42 and 43 °C with the sensor heads submerged in water.

Finally, two sensor heads were placed inside the incubator pre-set to 37 °C. The incubator was then set to 42 °C to simulate hyperthermia treatment.

Results

A total of 4 sensor heads were calibrated. Temperatures acquired always fell into the range of ± 0.1 °C and deviated less than 0.1 °C from the temperatures reported by the TP-200 and the mercury thermometer. Inside the incubator, the temperature measurements deviated by less than 0.4 °C from the temperature indicated on the display of the incubator during ramp-up. In this phase, the measurements were generally lagging the temperature on the display of the incubator. No overshoot was observed. Once the target temperature had been reached, measurements deviated less than ± 0.2 °C from the target temperature regardless of the sensor location (top/central tray, center/periphery of trays) inside the incubator.

Opening the glass door of the incubator even for a few seconds resulted in a substantial drop of temperature of several °C while the temperature indicated on the display of the incubator barely dropped. Opening only the metal cover (but not the glass door) for the same amount of time did not induce such an effect.

Discussion

The accuracy of the sensors as determined by the calibration was in line with the sensor specification. During ramp-up, the sensor requires some amount of time to heat up, hence the observed time lag. This effect grows stronger as thermal mass increases, such as with liquid of the cell cultures. In conclusion, the system has proven to be useful to gain confidence in the thermal accuracy and stability of the incubator; the effect on the biochemical processes can be assumed to be minimal. Furthermore, the live nature of the system allows for the recording of temperature profiles of the thermal exposure, which could be useful in studies that are accompanied by biochemical modelling and simulations.

References

Sapareto et al. "Thermal dose determination in cancer therapy." *Int. J. Rad. Onc. Biol. Phys.* 10.6 (1984): 787-800.

MULTISCALE 3D DATA VISUALIZATION FOR THE EXPLORATION OF BONE MECHANOMICS

Ariane C. Scheuren (1), Ryan M. Plett (1), Carly Taylor (1), Patrik Christen (1), Ralph Müller (1)

1. Institute for Biomechanics, ETH Zurich, Zurich, Switzerland

Introduction

Load-induced bone remodelling is a multiscale process mediated through complex interactions between multiple cell types and their mechanical environments. At the tissue scale, several mechanical parameters (e.g. strain energy density (SED), strain gradients and strain history related parameters) have been proposed to induce bone formation. However, the relationships between the diverse mechanical stimuli, the molecular responses of cells and bone remodelling remain poorly understood. Thereupon, the field of mechanomics is emerging, which aims to deepen our understanding of cellular responses to multiple types of mechanical stimuli [Wang, 2014]. Based on a platform, known as Local *in vivo* Environment (LivE) imaging, that combines end-point serial histology with micro-finite element (μ FE) analysis based on time-lapsed *in vivo* micro-computed tomography (μ CT) [Trüssel, 2015; Taylor, 2016], we propose an extension to the field of mechanomics to spatially resolved *in vivo* mechanomics in bone. The integration of 3D structural and diverse mechanical information at the tissue scale and protein level data at the molecular scale into one single 3D visualization provides the possibility to map the mechanome of single cells *in vivo*.

Methods

The 6th caudal vertebra of one female C57BL/6 mouse was cyclically loaded [Webster, 2008]. Time-lapsed *in vivo* μ CT (vivaCT 40, 10.5 μ m resolution) images were acquired weekly over 4 weeks, from which 3D dynamic morphometric parameters were derived [Schulte, 2011]. μ FE analysis was used to determine the SED distribution using ParOSol. The temporal (Δ SED_{max}) and spatial (∇ SED_{max}) gradients in SED_{max} were calculated according to the following equations:

$$\Delta SED_{max} = SED_{max}(t_3) - SED_{max}(t_1) \quad (1)$$

$$\nabla SED_{max} = \sqrt{\nabla x^2 + \nabla y^2 + \nabla z^2} \quad (2)$$

Finally, the vertebra was dissected and serially sectioned for staining using an anti-sclerostin antibody. Cells were mapped into the *in vivo* 3D volumes and the corresponding μ FE models [Trüssel, 2015]. A Python procedure was developed

to visualize the cellular protein level data within the 3D bone volume in ParaView (ParaView 4.3.1, Kitware Inc.).

Results

The LivE imaging platform was expanded to visualize single-cell protein level data within the 3D microenvironment (Figure 1). Using this approach, the merged data could be interactively explored in 3D and analyzed qualitatively by associating the protein levels to the dynamic morphometry and to the diverse SED maps, respectively.

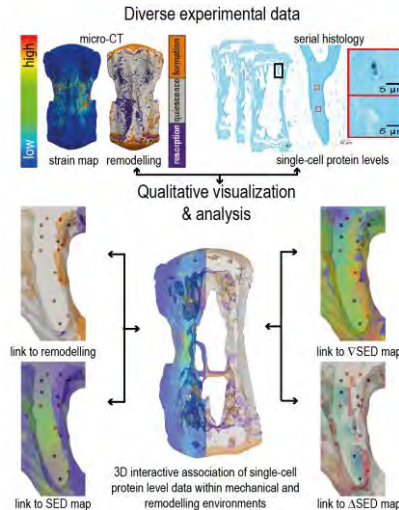


Figure 1: 3D qualitative visualizations of protein level data (sclerostin- cells in red, sclerostin+ cells in black) within dynamic morphometry and strain maps.

Discussion

The integration of 3D anatomical structures and the molecular information into one visualization provides an advanced tool to locally analyse the mechanome of single cells with respect to their 3D mechanical *in vivo* environment. Our current efforts focus on the ability to qualitatively and quantitatively assess the link between protein levels and the cellular *in vivo* environment in 3D.

References

- Schulte et al, Bone, 48:433-442, 2011.
- Taylor et al, Curr Dir Biomed Eng, 2(1): 449-453, 2016.
- Trüssel, Dr. sc., ETH Zürich, 2015
- Wang et al., Protein Cell, 2014
- Webster et al, Comput Methods Biomech Biomed Eng, 11:435-441, 2008.

INVESTIGATING LOCAL MECHANICAL REGULATION OF BONE HEALING IN AN IN VIVO MOUSE FEMORAL DEFECT MODEL

Duncan C Betts (1), Esther Wehrle (1), Gisela A Kuhn (1), Ariane C Scheuren (1), Graeme R Paul (1), Sandra Hofmann (1,2,3), Ralph Müller (1)

1. Institute for Biomechanics, ETH Zurich, Zurich, Switzerland; 2. Department of Biomedical Engineering; 3. Institute for Complex Molecular Systems, Eindhoven University of Technology, Eindhoven, The Netherlands

Introduction

The healing of bone defects is influenced by mechanical signals. The same is true, when a tissue engineered construct is implanted in the defect. However, the effect of the material on the mechanical environment in the defect is not well understood. Therefore, when testing materials in animal models, beneficial effects of a certain scaffold material might be masked by inappropriate mechanics. With an appropriate theoretical model for the mechanoregulation of the healing process, it might be possible to compensate for such effects by adjusting intrinsic properties of the scaffold or the stiffness of osteotomy fixation.

Aim

In this study, the role of defect size on the mechanical environment early in the healing process was investigated. We hypothesize that the level of strain energy density (SED) preceding ossification is independent of the defect size.

Methods

Two groups of female mice (C57BL/6) underwent a femoral mid-shaft osteotomy stabilised with an external fixator (MouseExFix, RISystem, Davos, Switzerland), one group (n=8) received a defect of 1.45 ± 0.16 (Mean \pm SD) mm, the second group (n=9) 0.85 ± 0.09 mm. The mice were scanned weekly using an *in vivo* micro-computed tomography system (vivaCT 40, Scanco Medical, Brüttisellen, Switzerland) providing a nominal resolution of 10.5 μ m. The images were registered, thresholded (395 mg HA/cm³) and sites of bone formation were determined by overlaying consecutive images. Based on the thresholded images micro-finite element models were generated by direct voxel conversion, assuming homogenous material properties for the individual elements with an elastic modulus of 14.3 GPa for bone and 3 MPa for non-bone [Simon, 2011]. An axial load of 10.5 N and a bending moment of 3.5 Nmm were applied to the fixator-bone construct. Using receiver operator characteristic (ROC) analysis, the optimal SED level for bone formation and area under curve (AUC) were determined.

Results

SED is a strong predictor of ossification in the first 3 weeks post osteotomy as demonstrated by a high AUC (Table 1).

	Week	AUC \pm SD (-)	SED \pm SD (MPa)
1.45	1	0.87 \pm 0.03	0.20 \pm 0.08
	2	0.87 \pm 0.02	0.19 \pm 0.05
	3	0.71 \pm 0.08	0.18 \pm 0.08
	4	0.58 \pm 0.15	0.00 \pm 0.00
0.85	1	0.83 \pm 0.07	0.31 \pm 0.18
	2	0.87 \pm 0.03	0.22 \pm 0.06
	3	0.78 \pm 0.09	0.08 \pm 0.06
	4	0.66 \pm 0.19	0.00 \pm 0.00

Table 1: Area under the curve and optimal SED for 1.45 mm and 0.85 mm defect group.

The AUC decreases with the progression of healing. This corresponds with the shift from repair to remodelling. The level of SED above which ossification occurred was not found to be significantly different between groups in weeks 1, 2 and 4. The significant difference between the groups in week 3 was due to the unequal progression of healing. In week 2 bridging was observed in 4 mice of the 0.85 mm group, whereas all mice in the 1.45 mm group were unbridged. The bridging stress shielded the soft tissue.

Conclusion

At sites of ossification, no significant differences in the pre-existing SED was found, thus confirming our hypothesis that the SED preceding and possibly provoking ossification is independent of the defect size. We recommend that future studies adapt either the stiffness of fixation or the scaffold design such that soft tissue in the defect receives an SED of at least 0.2 MPa.

Acknowledgements

Support from EU (BIODESIGN FP7-NMP-2012-262948) and the Swiss National Supercomputing Centre (CSCS).

References

Simon et al, CMBBE, 14:79-93, 2011.

WALKING COMPARISON BETWEEN PARTIAL AND TOTAL KNEE ARTHROPLASTY USING A MOVING FLUOROSCOPE

Thomas Zumbrunn (1), Pascal Schütz (1), Michi Angst (1), Fabian von Knoch (2), Stefan Preiss (3), Renate List (1), Stephen Ferguson (1)

1. Institute for Biomechanics, ETH Zürich, Switzerland; 2. Gelenkzentrum Zürich, Switzerland;
3. Schulthess Klinik, Switzerland

Introduction

The indication of joint arthroplasty has been increasing over the years resulting in younger, more active patients with higher expectations. Unicompartamental knee arthroplasty (UKA) offers a less invasive surgery than total knee arthroplasty (TKA) with anterior cruciate ligament (ACL) retention and partial preservation of the native joint articulation. Therefore, UKA is expected to address demands for improved knee function following joint arthroplasty. The aim of this study was to compare in vivo kinematics of patients with UKA and TKA implants during walking and deep knee bend (DKB) using fluoroscopy.

Methods

Level walking and DKB were analyzed for four UKA patients (3 male, 1 female) using a single plane moving fluoroscope. Each patient previously received medial UKA matching the native tibial slope with good clinical outcome. The moving fluoroscope tracked a subject's knee during overground walking, providing continuous x-ray images (Zihlmann, 2006). Five valid cycles per leg were recorded for each patient. In a separate study, six patients (5 male, 1 female) with contemporary TKA were analyzed using the same protocol for level walking. Through 2D/3D registration (Burckhardt, 2005) detailed kinematics between tibial and femoral implants were evaluated.

Results

Similar trends were found for knee flexion over the whole gait cycle between UKA and TKA patients. The UKA group showed higher implant flexion of 8.5° to 17.2° across the whole gait cycle compared to TKA implants (Figure 1). Internal/external rotation revealed a different trend between the two implants, showing substantially higher range of motion ($11.0^\circ \pm 5.9^\circ$ vs. $5.3^\circ \pm 2.8^\circ$) for the UKA group. During DKB the average of the reached implant flexion for UKA patients was $121.8^\circ \pm 3.6^\circ$ and both internal/external and abduction/adduction rotations remained constant throughout bending.

Conclusion

The overall greater flexion in the UKA group can be partially explained by differences in implant placement between TKA and UKA, however, the UKA group showed an increased range from mid-stance phase to maximum flexion of around 9° . There appeared to be a trend of increased internal/external rotation in contrast to TKA patients. Reduced range of knee rotation in TKA implants could be due to a missing ACL. During deep knee bend UKA patients achieved higher flexion than generally seen for TKA implants though smaller than native knees.

References

Burckhardt et al, IEEE Trans Med Imag, 24:676-88, 2015
Zihlmann et al, Gait Posture, 24:475-81, 2006

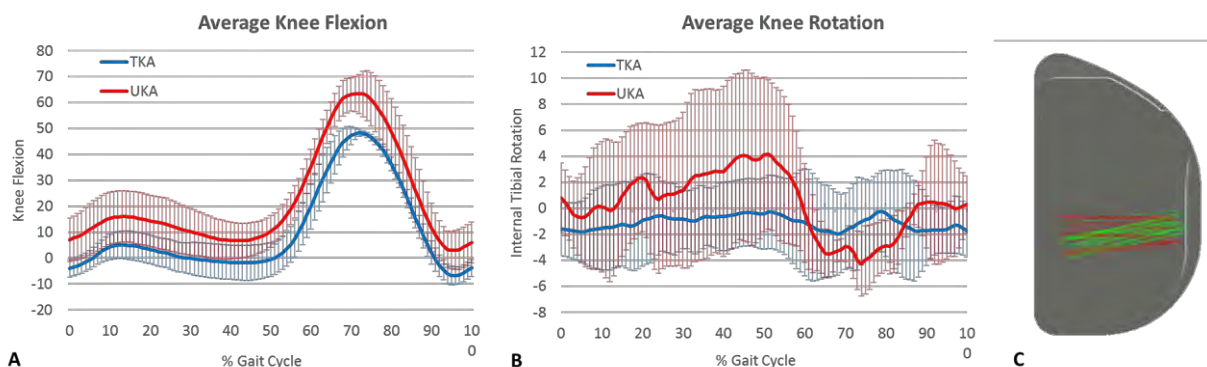


Figure 1: In vivo comparison of UKA and TKA kinematics for level walking: flexion/extension (A), internal/ external rotation (B) and projection of femoral axis onto tibia during stance (green) and swing (red) phase (C)

KINEMATICS ANALYSIS OF PARTIAL KNEE IMPLANTS: IN VIVO COMPARISON OF DIFFERENT ACTIVITIES

Adrian Roth (1); Lorena Suter (1); Fabian von Knoch (2); Stefan Preiss (3); Renate List (1); Stephen Ferguson (1); Thomas Zumbrunn (1)

1. Institute for Biomechanics, ETH Zürich, Switzerland; 2. Gelenkzentrum Zürich, Switzerland; 3. Schulthess Klinik Zürich, Switzerland

Introduction

Unicompartmental knee arthroplasty (UKA) has regained popularity as a treatment option for single compartment knee osteoarthritis. UKA has several advantages like early and rapid recovery, preservation of bone stock, lower complication rates and improved kinematic function compared to total knee arthroplasty (TKA). This leads to an improved range of motion and a more normally feeling knee following surgery. These improvements are primarily attributed to the retention of the anterior cruciate ligament (ACL) and the intact compartments of the knee joint following UKA. We hypothesized that there would be no difference in kinematics between knees with an implanted UKA and the contralateral native knees during daily activities.

Methods

Ten patients (8 male, 2 female; 67.2 yrs +/-9.8 yrs; BMI 25.3 +/-2.7) implanted with a contemporary medial UKA using standard surgical technique were analysed at least one year post-op. The ACL was determined intact and the tibial posterior slope matched the slope of the native bone. Each subject performed five valid trials of level walking and a deep knee bend (DKB) activity in our state of the art motion analysis laboratory. Additionally, nine patients also performed downhill walking on a ramp. All kinematics were based on the IFB Marker Set [List 2013], recorded with a 22 camera optoelectronic motion analysis system (VICON MX, Oxford, UK). Flexion/extension, internal/external rotation and abduction/adduction between tibia and femur were represented according to Grood and Suntay for daily activities.

Results

Nine out of ten subjects showed similar gait patterns for the UKA implanted and contralateral knee (Figure 1). Patient 1 showed around 14° lower max flexion angle during level walking for the implanted knee compared to the contralateral knee. The average of the measured maximum knee flexion angle during DKB for all implanted knees

was 118.5° +/-14.1° and the internal/external rotation range of the implanted knees was 9.3° +/-2.8°. Again, patient 1 showed a lower maximum knee flexion angle during DKB (95.1° +/-1.4°). Patients 2-10 also performed ramp descent, with a generally increased knee flexion of around 10° compared to level walking, showing similar motion patterns between the operated and non-operated leg (Figure 1).

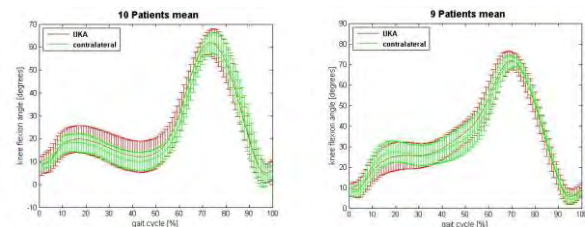


Figure 1: Knee flexion mean during level walking (left) and stair descent (right). The ipsilateral side with the UKA is in red and the contralateral side in green.

Conclusion

Most patients showed similar motion between the UKA implanted and contralateral native knee for downhill and level walking. The maximum flexion during deep knee bend was larger than what has previously been reported for TKA implanted knees during a lunge activity [Moro-oka, 2007], which supports the expectation that UKA can more closely match the function of native knees. Patient 1 showed lower maximum knee flexion and also reduced flexion during walking, even though, the flexion during walking (57.0° +/-3.5°) did not come close to the maximum flexion evaluated in deep knee bend (95.1° +/-1.4°). Unfortunately, we did not measure ramp descent for patient 1, due to technical difficulties during the measurements.

References

- List et al, J Strength Cond Res 27(6): 1529–1538, 2013.
- Moro-oka et al, Knee Surg Sports Traumatol Arthrosc, 15:93–99, 2007.

KINETICS OF MEDIAL UNICOMPARTMENTAL KNEE ARTHROPLASTY: COMPARISON TO CONTRALATERAL LEG

Lorena Suter (1), Adrian Roth (1), Fabian von Knoch (2), Stefan Preiss (3), Renate List (1), Stephen Ferguson (1), Thomas Zumbrunn (1)

1. Institute for Biomechanics, ETH Zürich, Switzerland; 2. Gelenkzentrum Zürich, Switzerland; 3. Schulthess Klinik, Switzerland

Introduction

For isolated compartmental osteoarthritis of the knee, unicompartmental knee arthroplasty (UKA) is a common treatment option, which replaces only the damaged compartment of the joint. Only around 8% of knee implants are UKAs although up to half of all patients are potential UKA candidates [Jones, 2016]. Some advantages of UKA are closer to normal biomechanics of the knee and greater postoperative ROM [Jones 2016; Longo, 2015]. The aim of this study was to compare the kinetics of different daily activities in patients with traditionally implanted medial UKA to the contralateral intact knee.

Methods

For the current study, 10 patients (8 male, 2 female; 67yrs +/-10yrs, BMI 25 +/-3) with contemporary, fixed bearing medial UKA following standard surgical technique were recruited at least one year postoperatively. The UKA was implanted matching the native tibial posterior slope and an intact ACL was confirmed. Our motion laboratory is equipped with a motion capture system and six integrated and two mobile (ramp and stair) force plates. Each subject had to perform five valid gait cycles during level walking, downhill walking (ramp descent) and stair descent for both legs. Ground reaction forces (GRF) normalized to body weight (BW) were recorded over the stance phase of each gait cycle.

Results

During level walking the second peak of the vertical GRF/BW was significantly ($p<0.05$) smaller for the UKA implanted leg (UKA: 1.05BW

+/-0.06BW, contralateral: 1.09BW +/-0.07BW). The decelerating impulse (integral in the first portion of stance phase) in the walking direction was significantly higher (132% +/- 15%) and longer (126% +/- 26%) for the implanted side during level walking. On the other hand, the accelerating impulse was significantly lower for the UKA implanted leg during level walking (65% +/- 22%) as well as for stair descent (65% +/- 34%). During stair descent the loading and unloading rate of the vertical GRF were significantly reduced for the implanted side (loading: 80% +/- 24%, unloading: 73% +/- 18%) (Figure 1).

Conclusion

The smaller second peak, loading and unloading rate of the vertical GRF for the implanted leg indicate that subjects tended to reduce load when pushing off and accepting weight with the operated leg during level walking and stair descent. The significantly lower impulse in walking direction of UKA implanted side resulted in a reduction of forward acceleration at the end of stance phase for level walking and stair descent. Additionally, in contrast to the contralateral native knee, the deceleration portion of the stance phase during level walking was longer (>50% gait cycle) than that of acceleration.

References

Jones et al, Orthop. Trauma, 31:8-15, 2017
Longo et al, Br. Med. Bull, 114:65-73, 2015

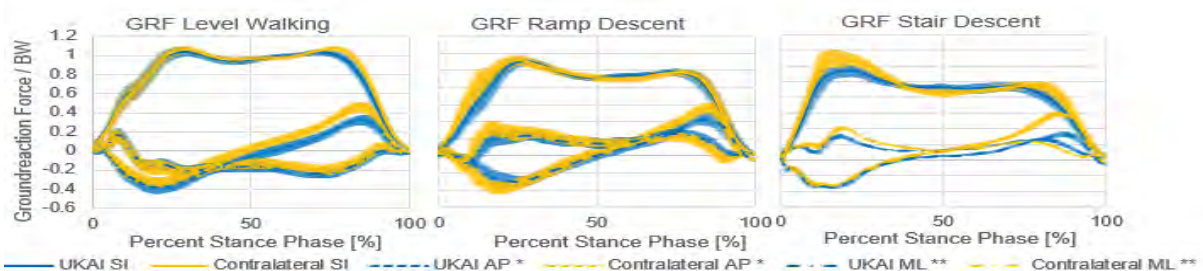


Figure 1: Average GRF for UKA implanted and contralateral legs during level walking, ramp descent and stair descent (SI= superior/inferior, AP= anterior/posterior, ML= medial/lateral, *= visualized threefold, **= visualized fivefold).

VALIDATION OF VIDEOFLUOROSCOPY TECHNIQUE FOR KINEMATIC ANALYSIS OF PARTIAL KNEE IMPLANTS

Luca Kiener (1), Thomas Zumbunn (2), Fabio D'Isidoro (2), Stephen J. Ferguson (2)

1. Department of Mechanical Engineering, ETH Zürich; 2. Institute for Biomechanics, ETH Zurich, Switzerland

Introduction

Videofluoroscopy is a frequently used technique to investigate the behavior of joint arthroplasties *in vivo*. Unlike in dual plane fluoroscopy, single plane fluoroscopy only takes an image from one perspective, which leads to a bigger error in the out of plane direction during the 2D/3D registration process [Zhu, 2012]. In this model matching process, a 3D model of the implant is placed to match its projection for each 2D videofluoroscopy frame. There are many sources of error, which have an influence such as a lower contrast between the surrounding tissue and the implant that limits contour visibility [Mahfouz, 2003]. Additionally, a discrepancy between the CAD model and the actual implant can lead to a mismatch [Kaptein, 2003]. The aim of this study was to provide a mechanism for the validation of our measurements using moving fluoroscopy.

Methods

In this study, UKA implants were fixed on Plexiglas cylinders with rigidly attached metal beads. From a CT scan of the cylinder a 3D Model of the implant with the beads was segmented. Various images of the cylinder/implant complex in different positions were taken with and without noise representing soft-tissue artefacts. A dynamic sequence was recorded from a lateral view. The usual matching procedure was applied to the implant shape without considering the beads. Then the 3D model of the implant with the beads was registered to each image, which was used as the "gold standard". The accuracy of the registration was evaluated comparing the six degrees of freedom with and without beads.

Results

The results show that there is a relatively large error in the out-of-plane direction. The highest error was observed for the out-of-plane direction of the tibial component (38.6 mm). For the femoral implant, the in-plane accuracy is the submillimeter area. The highest rotational error was seen for internal/external rotation. The other rotations were below 2° for both implants (Table 1).

	<i>In-plane</i> [mm]	<i>Out-of-plane</i> [mm]	<i>Rx</i> [°]	<i>Ry</i> [°]	<i>Rz</i> [°]
<i>Femoral</i>					
<i>No noise</i>	0.3	7.6	1.0	1.4	0.4
<i>Noise</i>	0.8	10.1	1.7	3.3	1.2
<i>Dynamic</i>	0.1	1.7	1.0	1.1	0.2
<i>Tibial</i>					
<i>No noise</i>	1.5	18.7	0.7	3.4	0.4
<i>Noise</i>	2.0	38.6	1.1	5.1	0.7
<i>Dynamic</i>	0.6	2.9	0.9	1.3	0.1

Table 1: Mean errors for *in vitro* tests with and without noise. In-plane and out-of-plane translational error. Mean rotational error for varus/valgus (Rx), internal/external (Ry) and flexion/extension (Rz).

Discussion

The out-of-plane error was expected to be large because of the missing information from the 2D image. The smaller accuracy in internal/external rotation could result from the fact that it is an out-of-plane movement and due to the lack of features that change with an increment in rotation. The data also showed greater deviation for images with simulated noise due to increased difficulty of the operator (Table 1).

References

- Kaptein et al, J Biomech, 36:873-82, 2003
- Mahfouz et al, IEEE TransMed Imaging, 22:1561-1574, 2003
- Zhu et al, Comput Methods Biomech Engin, 15:1245-56, 2012

FINITE ELEMENT MODELING OF A TROCHLEODYSPLASTIC KNEE; STRESS DISTRIBUTION IN THE PATELLOFEMORAL JOINT

Tobias Götschi (1) (2), Dominik Kaiser (2), Elias Bachmann (1) (2), Jess G. Snedeker (1) (2), Sandro F. Fucentese (2)

1. Institute for Biomechanics, ETH Zurich, Switzerland; 2. Balgrist University Hospital, University of Zurich, Switzerland

Introduction

Instability of the patellofemoral joint related to trochlear dysplasia can be successfully treated by sulcus deepening trochleoplasty. The cartilage is peeled off, the groove is deepened and lateralized in the shape of a V and the cartilage is pressed into the newly formed groove. Complications, often associated with degenerative changes and retropatellar pain, have been reported following the surgery [Bollier, 2011]. In the present study it was hypothesized that an incongruence between the osseous components of the patellofemoral joint created by the sulcus deepening trochleoplasty results in increased cartilage stress, possibly leading to chondral degeneration and pain.

Methods

Using magnetic resonance imaging, surface models of a healthy and a trochleodysplastic knee were developed. The trochleodysplastic knee underwent virtual sulcus deepening osteotomy with varying lateralization and deepening of the trochlear groove. Patellofemoral kinematics were computed using a transient finite element simulation with prescribed tibiofemoral kinematics (Fig. 1). Cartilage stress profiles were predicted at 30°, 45°, 60° and 75° of knee flexion both pre- and postoperatively. The patellar and femoral cartilage peak and mean contact pressure as well as the peak and mean Von Mises equivalent stress at the chondro-osseous interface were analysed.

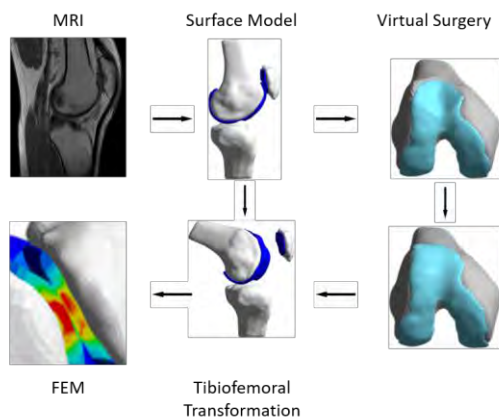


Figure 1: Flow chart of the FE model development incorporating multimodality data.

Results

The osteotomized knee exhibited greater peak and mean contact pressure as well as peak and mean Von Mises equivalent stress compared to the healthy knee model and the preoperative state over all measured flexion angles. The effect was more pronounced for lower knee flexion angles (Fig. 2). Cartilage to cartilage contact area decreased postoperatively by up to 27%.

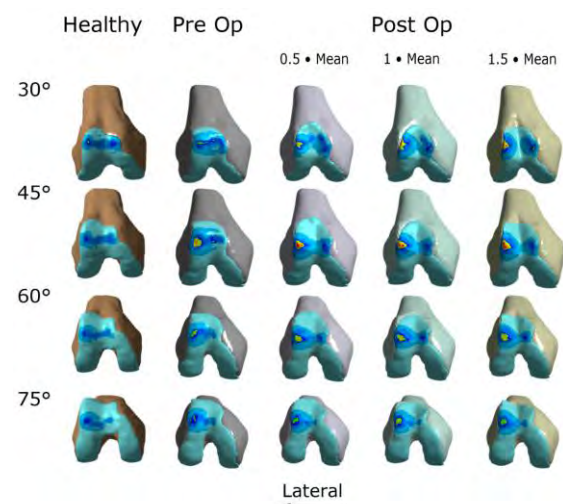


Figure 2: Contact pressure patterns for the healthy and the dysplastic knee pre- and postoperatively with different surgical parameters at different knee flexion angles.

Discussion

Based on the findings of the current study, it is plausible that sulcus deepening trochleoplasty may be a risk factor for increased patellofemoral joint stress attributed by reduced contact area as well as geometric incongruence. This may have clinical relevance as increased patellofemoral joint stress has been linked to a higher risk of patellofemoral pain [Farrokhi, 2011] and osteoarthritis [Buckwalter, 2013].

References

- Bollier et al, JAAOS, 19:8-16, 1985.
- Buckwalter et al, Cartilage, 4:286-294, 2013.
- Farrokhi et al, Osteoarthritis and Cart, 19:287-294, 2011.

IDENTIFYING THE ROLE OF FOCAL ADHESIONS AND THE NUCLEUS IN CELLULAR TENSILE STIFFNESS: A FINITE ELEMENT APPROACH

Aron Horvath (1,2), David Flückliger (1,2), Unai Silvan (1,2), Jess Snedeker (1,2)

1. Institute for Biomechanics, ETH Zurich, Switzerland; 2. Balgrist University Hospital, University of Zurich, Switzerland

Introduction

The whole cell mechanical resistance to tension involves numerous “links” in the physical chain, from the elastic properties of the substrate itself, to the ligand conformation on the substrate, to the focal adhesion complexes that link to the extracellular environment via integrins or other transmembrane proteins, and finally to the actomyosin machinery that enables cell contractility and nucleus deformability through the LINC complexes. We have developed a functional imaging platform built around a modified commercial stretching device that incorporates a stiffness-tunable silicone substrate to provide a controlled, homogeneous, biaxial tensile strain to cultured cells [Bartalena, 2011]. The deformation beneath and surrounding the cell is determined by the displacement of fluorescent beads covalently bonded to the surface of the substrate. Using images of the beads both before and after mechanical stretching, maximum strain drop (MSD) is calculated, which is the difference between the minimum strain beneath the cell body and the average strain experienced by the cell. Furthermore, tensile cell stiffness is then estimated with an inverse finite element model based on the ability of the cell to resist the applied substrate deformation. In this study, we exploit this in-silico model to parametrically investigate the relative contributions of cellular compartments to whole cell mechanical resistance/adaptation through dynamic substrate stretching.

Methods

We have implemented a three-dimensional finite element model in which the impact of the experimental conditions, e.g. substrate stiffness and strain extent, on the modelled cell can be explored. It simulates the cell in biaxial tension as the cell is coupled to the substrate and predicts the MSD. The model of the cell is composed of geometrically and mechanically (linear elastic) defined and parametrically investigated cytoplasm (cell shape) (Figure 1.), focal adhesion points and a nucleus, for which the stiffness was set to be 4 times stiffer than the cytoplasm [Milner, 2012]. The focal adhesions were simulated with combinations of three different sizes and different distributions within the cell area. Three different cell shapes (elongated, spherical and “realistic”) each of two different sizes have

been analysed. To test the influence of the size and the orientation of nucleus, two different sizes and three different orientations (0, 45, 90 degrees) were implemented.



Figure 1: Simulated cell shapes. Spread, elongated and circular. Scale bar 40 μ m.

Results

The simulated and calculated MSD values show clear differences, which are dependent on the various cell shapes. The presence and size of the nucleus greatly influence the MSD but its orientation has a minor effect on the overall outcome. We found that the spatial distribution and quantity of focal adhesions alter the MSD in different manners. However, increasing the cytoplasm/nucleus stiffness results in decreasing effects of the focal adhesions and the nucleus orientations on the MSD.

Discussion

The designed in-silico experimental approach is well suited for deciphering the contribution of the different cell components to the overall quantified MSD values. In these simulations, while we have observed that the nucleus has a huge impact on the predicted MSD values, the focal adhesions only have a mild influence on the outcome. However, our model assumes uniform material properties of the individual components, and that the connections between the different parts are also simplified. The model validation with appropriate and targeted experiments is ongoing.

References

- Bartalena G. et al, J Biomed Micro, 13:291-301, 2011.
- Milner JS. et al, J Funct Biomater, 1:209–224, 2012.

STIMULATION OF PRIMARY HUMAN OSTEOBLASTS WITH THE BMP ANTAGONISTS NOGGIN, GREMLIN1/2 AND CHORDIN

Rahel D May¹, Daniela A Frauchiger¹, Lorin M Benneker², Sandro Kohl² & Benjamin Gantenbein¹

¹ Tissue and Organ Mechanobiology, Institute for Surgical Technology and Biomechanics, University of Bern, Bern, Switzerland

² Department of Orthopaedic Surgery and Traumatology, Inselspital, Bern University Hospital, University of Bern, Bern, Switzerland

Introduction

A possible explanation of pseudarthrosis after spinal fusion could be a secretion of BMP antagonists by IVD cells, which were not removed during discectomy. The BMP pathway plays a crucial role in bone turnover by inducing osteogenesis. BMP antagonists like Noggin (NOG), Gremlin1/2 (GREM1/2) and Chordin (CHRD) hindering bone formation by inhibiting the BMP pathway (1).

We hypothesized that human primary osteoblasts (OB) stimulated with NOG, GREM1/2 and CHRD show an inhibition of the osteogenic phenotype.

Methods

OB were isolated from patients undergoing total knee replacement (average \pm SEM, 40 ± 14). Cells were cultured in monolayer up to passage two to minimize dedifferentiation effects. All protocols involving human tissue were ethically approved. OB were seeded at a density of 10^4 cells/cm². OB were stimulated with 5/500/1000 ng/mL NOG, GREM1/2 and CHRD respectively. Cytokines were applied with osteogenic medium or α -MEM both supplemented with 100 ng/mL BMP-2. The respective medium for each experimental group was refreshed twice per week. After 21 days of culturing in hypoxic conditions (2% CO₂), matrix mineralization of OB monolayers was measured by Alizarin red (ALZR) staining. ALZR was quantified by absorbance and normalized to cell activity (Resazurin assay). Furthermore, was measured the alkaline phosphatase (ALP) activity after 10 and 21 days.

Results

After 21 days, an increase of ALZR staining of mineralized matrix was observed in the OB culture in osteogenic medium compared to OB grown in control medium. OB stimulated with α -MEM supplemented + 100 ng/mL BMP-2 showed no calcium deposition. Groups stimulated with osteogenic medium + 100 ng/mL BMP-2 showed

an increased matrix mineralization. Only groups stimulated with GREM2 and CHRD showed a trend to have a lower calcium deposition, whereas matrix mineralization seems to be increased in OB stimulated with NOG and GREM1.

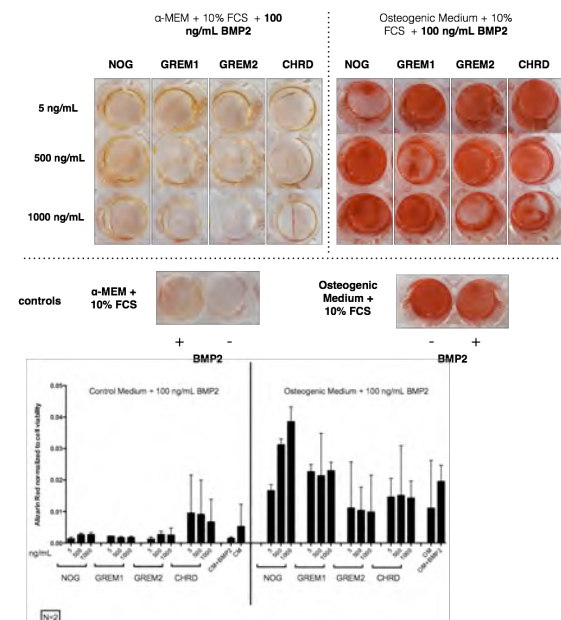


Figure 1: Alizarin red staining (top) and quantification (bottom) of osteoblasts.

Conclusions

We could not confirm our hypothesis that the exogenous stimulation of primary adult human OB with BMP antagonists will lead to an inhibition of the osteogenic phenotype and in this sense to a reduction of matrix mineralization.

Acknowledgements

This study was supported by direct funds from Hansjörg Wyss and Hansjörg Wyss Medical, US.

References

Chan et al, Arthritis Res Ther 18, no. 1, 2015

MINIMISING EXTERNAL FIXATOR STIFFNESS VARIATION VIA COMPUTATIONAL ANALYSIS

Graeme R. Paul (1), Mathias Cherbuin (1), Esther Wehrle (1) and Ralph Müller (1)

1. Institute for Biomechanics, ETH Zurich, Zurich, Switzerland

Introduction

An important parameter in the process of bone fracture healing is the stiffness of the fixation method [1]. This stiffness directly affects the inter-fragmentary movement leading to changes in the healing process [2]. Hence, the stiffness of the fixation system has a direct effect on the formation and healing of bone. Due to this, in preclinical studies the use of controlled and standardised fixation systems is crucial. In such studies, the fixation stiffness is assumed to not vary between animal groups. To ensure this, we conduct *ex vivo* stiffness tests of the fixation system to enforce minimal variance between the external fixators chosen for the studies. However, some inter- and intra-fixator stiffness variations have been noted. The following work outlines a computational approach with the purpose of investigating variation in the fixator stiffness with the intention of reducing variation in *in vivo* experiments.

Methods

Four external fixators manufactured by RISystem (Davos, Switzerland) were implanted into 2mm diameter PMMA cylinders ($E = 2.3\text{GPa}$), as seen in Figure 1. The body of the fixator was constructed out of PEEK ($E = 3.8\text{GPa}$), while the pins were made out of a Titanium Aluminium Niobium alloy (TAN) ($E = 114\text{GPa}$). The fixators were then compressed with a load of 1N using a Zwick Z005 mechanical testing system (Ulm, Germany). This process was repeated 3 times for each fixator.

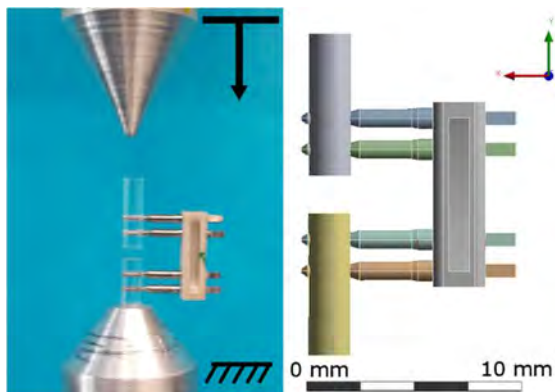


Figure 1: Experimental Setup (left), 3D representation of arrangement (right)

From this arrangement a 3D model was generated to replicate the experimental arrangement (Figure 1). In the simulation, a uniaxial load of 1N was applied to the top PMMA cylinder, while it was fixed at its distal end. This model was solved using the finite element method in ANSYS® Academic Research, Release 18 (Canonsburg, USA). Parameters of material properties and pin placement geometries (i.e. the number of threads inserted) were then varied to try capture inter- and intra-fixator variations.

Results

The computational model predicted a stiffness of 24.64N/mm, with experimental results showing a mean of $23.83 \pm 0.77\text{N/mm}$. The computational study showed that a large part of the variation can arise from pin placement. This relationship can be described (R^2 error = 0.90) with the following formula, where k is the external fixator axial stiffness:

$$k = 24.40 - 0.70x_1 - 0.78x_2 - 0.33x_3 - 0.46x_4$$

x represents the distance (in mm) between the fixator body surface and the end of the pin thread (where pin 1 is the upper most, pin 4 being the lower most pin). It was also shown that Young's moduli variation in the material has a significant effect on the stiffness, described (R^2 error = 0.99) by the following formula:

$$k = -0.28 + 3.4E_{PEEK} + 2.24E_{PMMA} + 0.05E_{TAN}$$

Conclusion

Empirical variance in intra-fixator stiffness measurement can be accounted for, primarily, in pin positioning and, for inter-fixator stiffness, in variation of material parameters. This underlines the importance of ensuring pins are correctly screwed in the fixator to preserve stiffness measurements between *ex vivo* and *in vivo*. Finally, forces experienced within the fracture region are most likely not completely uniaxial, hence including appropriate non-uniaxial loading in experimental and computation models would provide greater insight on fixator behaviour.

References

1. Gardner et al, J. Orthop. Sci., 16(3):298-303, 2011.
2. Mark et al, Clin. Orthop. Relat. Res., 419:245-250, 2004.

COMPUTATIONAL FLUID DYNAMICS MODELLING OF STENTED CORONARY ARTERIES

Patrick Bischof (1), Christian Lipp(1), Daniel Brunner(1) and Dirk Wilhelm(2)

(1) Institute of Computational Physics, ZHAW, Zurich University of Applied Sciences, 8400 Winterthur, Switzerland

(2) Institute of Applied Mathematics and Physics, ZHAW, Zurich University of Applied Sciences, 8400 Winterthur, Switzerland

Abstract

Stents are medical implants deployed in a blood vessel in order to prevent blockage of e.g. an artery. It is well established that these medical devices can lower the risk of numerous heart diseases like Stenosis, thrombosis and transient ischemic attacks. However, there are remaining side effects that have to be dealt with. An emerging in-stent restenosis leads to a reduction of the blood flow rate, which causes the reoccurrence of the initial problem under different circumstances.

High changes of wall shear stress (WSS) within the stent in symbiosis to areas of low WSS (0-0.4Pa) can provoke accelerated growth of scar tissue [1]. The objective of the present work is comparing the WSS using Computational Fluid Dynamics Simulations (CFD) under different conditions. Thereby, various simulations have been conducted for different geometries and strut thicknesses. The blood was represented by either a Newtonian or Non-Newtonian model. In addition, basic Fluid-Structure-Interaction study of an artery has been conducted.

Numerical results confirm the shear thinning behaviour of Carreau fluids during the whole cardiac cycle. A maximal relative difference of 28% in WSS was found between Non-Newtonian and Newtonian model, whereas the Newtonian stresses were consistently higher. Furthermore, it is shown that reduction of strut thickness by 50% increases average WSS along stented blood vessel regions up to 50%. This behaviour is helpful especially at vessel regions close to stent struts. The comparison between different stent geometries shows that it is favourable to minimize the area of stent struts. In particular, the area exposed to low WSS (0 to 0.4 Pa) is smaller at stent geometries with minimized strut areas.

Furthermore, it is shown that steady-state solution of average WSS deviates less than 5% in comparison to the transient results. Moreover, this simplification drastically reduces the computational effort, thus the remaining capacity can be used for parameter studies of further optimizations. The Fluid-Structure-Interaction model has been implemented on a basic level, but the computational

effort increase dramatically compared to the static model. Moreover, no significant advantages compared to the static models could be revealed so far.

Figures

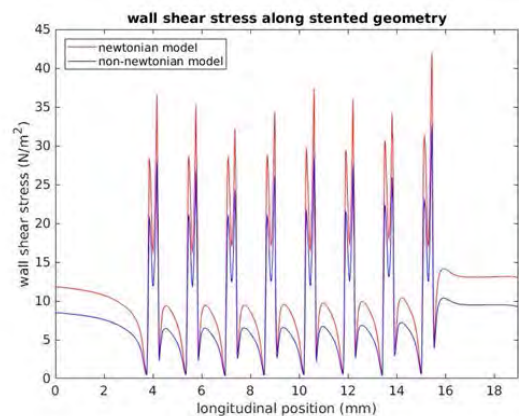


Figure 1: Wall shear stress of different viscosity models along stented geometry.

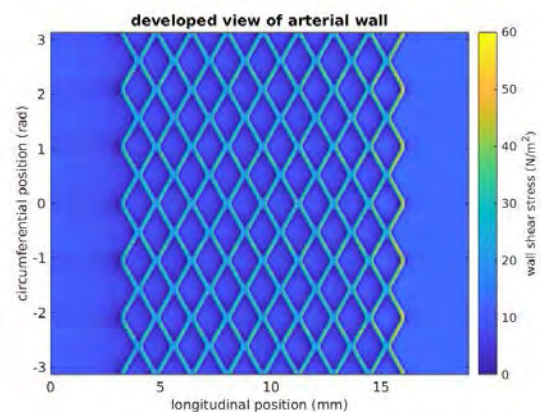


Figure 2: Developed view of arterial wall with deployed stent. Peak of WSS along inlet side.

References

[1] Qiao, A. Zhang, Z. Numerical Simulation of Vertebral Artery Stenosis Treated With Different Stents, ASME J. Biomech. Eng., 136(4): 041007, 2014.

SOFT AND NANO-STRUCTURED METAL ELECTRODES FOR FLEXIBLE ELECTRONICS

Bekim Osmani, Tino Töpfer, Gabriela Gerganova, Hans Deyhle, and Bert Müller

Biomaterials Science Center, Department of Biomedical Engineering, University of Basel, Gewerbestrasse 14, 4123 Allschwil, Switzerland.

Introduction

Soft electrodes are essential components of thin-film dielectric elastomeric transducers alias artificial muscles and flexible electronics [Rosset, 2016]. One can increase its compliance by manipulating the intrinsic material properties or by introducing structural features, such as wrinkles or ripples, on the top layer [Schweikart, 2009]. Wrinkling occurs when a compressed stiff film is attached to a softer substrate [Osmani, 2017]. Here, we demonstrate the fabrication of soft and nano-structured gold electrodes on wrinkled viscous silicone (PDMS) films with a thickness of several hundred nanometers.

Methods

Vinyl-terminated PDMS (V05, Gelest, Inc., Morrisville, PA, USA) with a molecular weight of 800 g/mol was spun at speeds of 3,000 and 7,000 rpm for two minutes (WS 400B-6NPP/LITE/AS, Laurell Technologies Corporation, North Wales, PA, USA) onto 2-inch silicon wafers (SIEGERT WAFER GmbH, Germany) to get PDMS films with thicknesses of (600 ± 150) and (300 ± 75) nm. The thickness and topology of the PDMS films was determined using atomic force microscopy (AFM) in tapping mode.

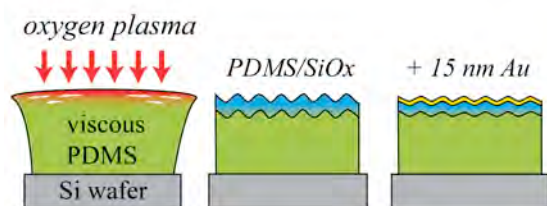


Figure 1: Schematic of plasma treated PDMS film with a reduced wrinkling amplitude after sputter deposition of the Au electrode.

The specimens were oxygen plasma-treated at 200 W for 144 s, with a frequency of 40 kHz (PICO System, Diener Electronics, Ebhausen, Germany). The application of an oxygen plasma treatment alters the surface morphology as schematically shown in Figure 1. Au electrodes with a thickness of 15 nm (Lesker, East Sussex, UK) were sputtered using a DC sputter coater (SCD040, Balzers Union, Liechtenstein) at a discharge current of 15 mA. The Ar pressure was kept at 0.05 mbar (Carbagas AG, Gumligen, Switzerland).

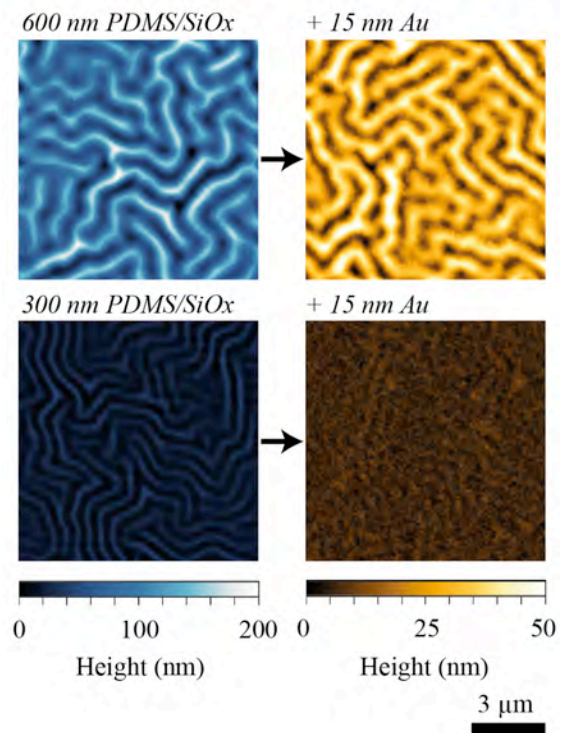


Figure 2: The amplitude of the wrinkled PDMS film is reduced by a factor of 4 after sputter deposition of 15 nm Au.

Results and Discussion

We have fabricated soft and nanostructured Au electrodes on viscous nanometer-thin PDMS films. Oxygen plasma treatments enables tuning of the amplitude and periodicity of the nanostructured films. The film thickness plays a crucial role in the formation of these nanostructures. The amplitudes of surface wrinkles on 600 and 300 nm PDMS films were found to be 200 and 50 nm, respectively. After the sputter deposition of 15 nm Au the wrinkling amplitudes were reduced in both cases by a factor of four.

Acknowledgements

The financial support of the nano-tera.ch initiative as well as the Swiss Nanoscience Institute (SNI) for the financial contribution to the AFM is gratefully acknowledged.

References

- Rosset et al., Appl. Phys. Rev. 3 (3), 031105, 2016.
- Schweikart et al., Microchim. Acta 165, 249-263, 2009.
- Osmani et al., Eur. J. Nanomed. 9(2):69-77, 2017.

ARTIFICIAL MUSCLES TO TREAT SEVERE INCONTINENCE

Bert Müller (1) Bekim Osmani (1), Gabor Kovacs (2), Tino Töpper (1), Simone E. Hieber (1)

1. Biomaterials Science Center, Department of Biomedical Engineering, University of Basel, Switzerland; 2. Laboratory of Mechanical Systems Engineering, Empa Dübendorf, Switzerland

Introduction

In our aging society, an increasing number of people suffer from severe urinary and faecal incontinence. This prevalence has a considerable economic impact, but is generally underestimated, see e.g. [Stoker, 2001].

In severe cases of incontinence, artificial sphincter systems are considered as a valid option, see e.g. [Fattorini, 2016]. Systems used today are fluid-filled cuffs, but do not provide a reliable solution, as many complications occur, including wound infections, post-operative pain, tissue erosion and atrophy.

As a consequence, research teams around the world try to develop systems that better mimic the natural counterpart. The artificial muscle should have integrated sensory feedback, as given by our nerve system. It should act in milliseconds to also address stress incontinence. The energy to supply the muscles should ideally be generated within the body. Herein, we report on the possible solutions for such a smart implant.

Physical principles for sphincter

Currently, the surgeons can only purchase and implant devices that are based on fluid-filled cuffs. Prototype devices based on shape memory alloys have been proposed and realized, but the power consumption and the speed of operation are serious drawbacks. Devices based on electrically driven motors are less power consuming and are in clinical trial, e.g. by Myopowers SA. Nevertheless, they do not reach the time response required to successfully treat stress incontinence. Therefore, our team has proposed the usage of dielectric elastomer transducers that have many advantages including high efficiency, millisecond response time, and integrated sensory feedback as these transducers can work as actuator and sensor simultaneously [Müller, 2009]. The only drawback is the operating voltage of several hundred volts. Therefore, we developed thin-film techniques to fabricate nanometre-thin sandwich structures, which will allow working at voltages given by common battery [Töpper, 2015]. There are two challenges. First, we have to obtain homogeneous nanometre-thin elastomer films, and second, soft electrodes have to be realized [Osmani, 2017].

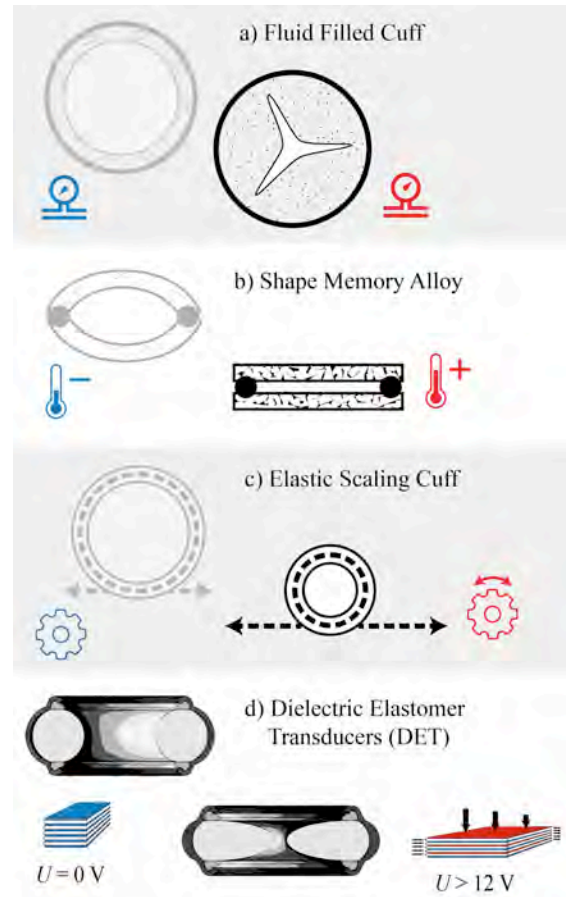


Figure 1: Selected working principles for artificial sphincters which are currently under development.

Acknowledgements

This project was funded by the nanotera.ch initiative with collaboration partners from the Biomaterials Science Center (BMC) at the Department of Biomedical Engineering of the University of Basel, the Swiss Federal Laboratories for Material Science and Technologies (Empa), the Institute for Surgical Technology and Biomechanics (ISTB), Kantonsspital Schaffhausen, Kantonsspital Winterthur and Inselspital Bern.

References

- Stoker et al, *Radiology*, **218**:621–641, 2001
- Fattorini et al, *Ann. Biomed. Eng.*, **44**:1355–1369, 2016.
- Töpper et al, *Sens. Actuators A*, **233**:32, 2015.
- Osmani et al, *Proc. SPIE*, **10163**:101631E, 2017.

A NOVEL BIOMIMETIC IN VITRO MODEL TO STUDY OSTEOCYTE MECHANOBIOLOGY USING MICRO-3D PRINTING

Felicitas R Flohr (1), Ralph Müller (1)

1. Institute for Biomechanics, ETH Zurich, Zurich, Switzerland

Introduction

Osteocytes are considered as the professional mechanosensory cells in bone. *In vivo*, they are tightly confined in the lacuno-canalicular network (LCN) surrounded by the stiff bone matrix. While this three-dimensional (3D) environment has been shown to be an important aspect in osteocytic mechanosensing *in vitro* [Bacabac, 2008] as well as *in vivo* [Vatsa, 2008], its influence remains poorly understood due to a lack of suitable experimental systems.

To overcome this limitation, we present a proof of concept study for a novel *in vitro* osteocyte model. This system employs micro-3D printed cavity and channel structures mimicking the LCN [Flohr, 2017] and allows live-cell fluorescence microscopy.

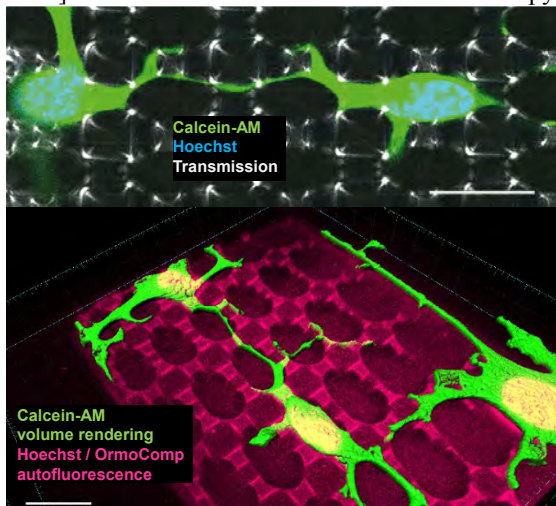


Figure 1: A Fluorescence micrograph and B 3D visualization of IDG-SW3 cells in micro-3D printed structure. Scale: 20 μm .

Methods

Structures mimicking the LCN were micro-3D printed by two-photon polymerization with the Nanoscribe Professional GT (Nanoscribe GmbH, Germany) using inorganic-organic hybrid polymer OrmoComp[®], an (micro resist technology GmbH, Germany). IDG-SW3 osteocytes (Kerafast Inc., USA) were differentiated for 35 days before dissociation and reseeded on printed structures. Cells were stained with Calcein-AM (Sigma-Aldrich, Switzerland) and Hoechst (Chemodex, Switzerland) and imaged on an upright confocal microscope (Zeiss LSM880, Germany).

Results

IDG-SW3 osteocytes could be cultured in the printed LCN-mimicking structures for over 96 hours. We observed that osteocytes grew inside the cavities and extended multiple processes through the channels, leading to cell-cell-contacts (Figure 1A). We are able to obtain high-resolution confocal images of live osteocytes (Figure 1B) and time-lapse images of the dynamics of cell bodies and nuclei over several hours (Figure 2).

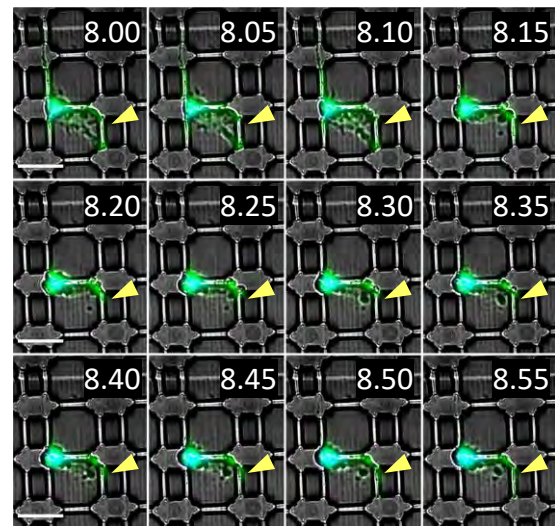


Figure 2: Excerpt from a time-lapse image series of IDG-SW3 cell retracting and extending a process through a micro-3D printed channel. Green: Calcein-AM, blue: Hoechst. Scale: 20 μm .

Discussion

We established a novel 3D *in vitro* model in which osteocytes can be cultured and observed long-term in a biomimetic 3D environment. We believe that this system opens up new avenues for research in osteocyte mechanobiology: Micro-3D printing allows for tight control over the geometry of the cellular environment. In combination with functional readouts attainable through live-cell microscopy, open questions can be addressed, for example pertaining to the influence of lacunar shape on osteocytic mechanosensation.

References

- Vatsa et al, Bone, 43:452–8,2008.
- Bacabac et al, J Biomech 41:1590–8, 2008.
- Flohr et al, Calcif. Tiss. Int., 100:S49, 2017.

MECHANICAL AND BIOLOGICAL CHARACTERIZATION OF 3D PRINTED POLYMER LATTICES FOR BONE TISSUE ENGINEERING

Paul F. Egan (1), Xiuyu Wang (1), Helen Greutert (1), Kristina A. Shea (2), Karin Würtz-Kozak (1), and Stephen J. Ferguson (1)

1. Institute for Biomechanics, ETH Zurich, Switzerland; 2. Engineering Design and Computing Laboratory, ETH Zurich, Switzerland

Introduction

Advances in additive manufacturing are enabling the design and fabrication of complex 3D printed structures suitable as biomaterials for tissue engineering, such as beam-based lattices [Wild et al, 2017]. Beam-based lattices have favourable mechanical properties due to greater mechanical efficiency at a given porosity when compared to more common foam-based scaffolds [Egan, Ferguson, Shea, 2017]. Experiments and simulation are necessary for characterizing diverse lattice designs to determine their performance as biomaterials for bone tissue engineering.

Methods

Lattices were designed with python scripting and Abaqus software to generate structures with controlled beam diameters, unit cell size, and porosity. Lattices were manufactured with a Stratasys Objet Connex polyjet printer with MED610 material. Support material was removed from structures chemically to reduce structural damage during cleaning. Scaffolds were sterilized and seeded with SAOS-2 cells that are representative of a bone tissue engineering environment [Sobral et al, 2011]. Light microscopy and confocal laser scanning microscopy were used to image scaffold structure and cell growth.

Tissue growth simulations were conducted in a voxel environment representing one eighth of a lattice unit cell of 50% porosity. A scanning mask was used to calculate local curvature, tissue voxels were added in locations with positive curvature, and the simulation ran until structures were filled [Bidan et al, 2013]. Finite element analysis (FEA) for properties relative to the base polymer used beam-based models in Abaqus [Egan et al, 2017].

Results

Scaffolds were designed with 500 μ m beam diameters and 500 μ m diameter interconnectivity pores. Manufactured beams diameters were measured in the range of 400 μ m-600 μ m. Tissue grew on surfaces for both topologies (Fig. 1).

Simulations suggest the FX-BC topology facilitates faster tissue growth and has a higher shear modulus, but lower elastic modulus than the Cube topology (Fig. 2)

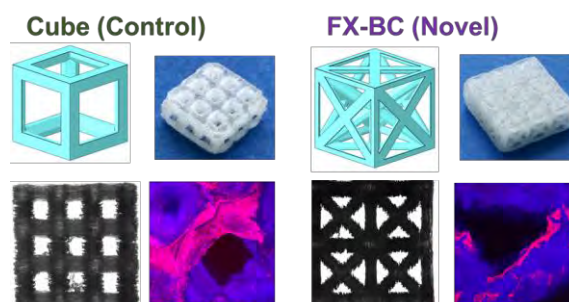


Figure 1: Cube/FX-BC topologies; panels (clockwise) show CAD design, 3D prints, structural microscopy, and 6 week SAOS-2 tissue growth.

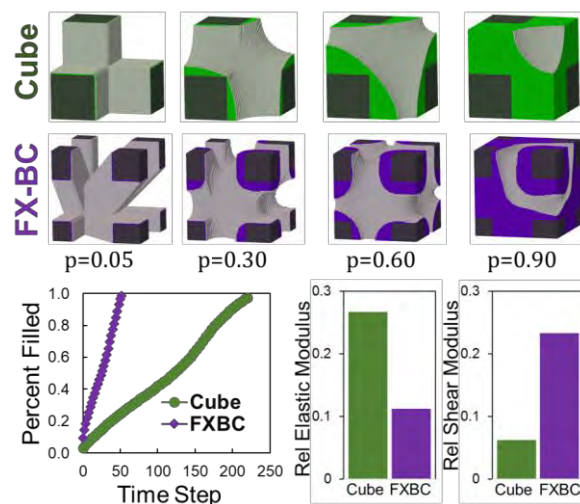


Figure 2: Tissue growth simulation and plots for Cube/FX-BC topologies with percent filled tissue p . FEA for Elastic/shear moduli of $p=0$ structures.

Discussion

Both topologies were manufacturable and supported tissue growth, thus suggesting their suitability as tissue scaffolds. Simulations suggest lattices of different topologies provide contrasting properties that influence mechanical and biological performance. Further experiments are required to determine manufacturing/simulation accuracy and support lattice optimization as biomaterials.

References

- Bidan et al, Comp Meth Biomech, 16:1056, 2013.
- Egan, Ferguson, Shea, J M Des, 139:061401, 2017.
- Sobral et al, Acta Biomater, 7: 1009, 2011.
- Wild et al, 3DP and Add Manu, 4:143, 2016.

OPTIMIZATION OF 3D PRINTED HYDROGELS WITH PRIMARY ANTERIOR CRUCIATE LIGAMENT CELLS FOR TISSUE ENGINEERING

Ezgi Bakirci¹, Andreas Hugi², Sufian S. Ahmad³, Sandro Kohl³, Olivier Guenat² & Benjamin Gantenbein¹

¹Tissue and Organ Mechanobiology, Institute for Surgical Technology and Biomechanics, University of Bern, Bern, Switzerland,

²Artorg Center for Biomedical Engineering, Organs-on-Chip Technologies, University of Bern, Bern, Switzerland

³Department of Orthopedic Surgery and Traumatology, Insel Hospital, University of Bern, Bern, Switzerland

Abstract

We here report on a tissue engineered Anterior Cruciate Ligament (ACL) scaffold fabricated using 3D bioprinting technology. The aim of this *in vitro* study was to optimize the printing parameters for maximum cell viability, determinate cellular response and characterize mechanical properties of materials. Human ACL cells were used as constituent cells and mixture of gelatin, fibrinogen and hyaluronic acid were used as cell-laden hydrogel. Cell localization and proliferation were investigated to study cell functions and tissue formation process in 3D structure.

Introduction

ACL is most commonly injured ligament of knee (1). It does not heal due to poor healing potential and limited vascularization. Therefore, surgical intervention is usually used and several ACL reconstruction surgeries are performed different grafts. However, the long-term clinical outcomes showed that grafts were suboptimal due to poor abrasion resistance and limited integration between grafts and host tissues. These outcomes have prompted a growing interest in tissue engineering solutions for ACL reconstructions.

The aim of this study was to optimize *in vitro* 3D bioprinted scaffold design for ACL tissue engineering. We focused on material selection and printing parameters based on cellular response and mechanical properties of materials.

Material and Methods

ACL scaffolds were produced using 3D Discovery® RegenHU bioprinter equipped with three different print heads. The diameter of scaffolds was 3 mm and the height was 0.5 mm. Bioink solution includes gelatin (35 mg/ml), fibrinogen (25 mg/ml) and hyaluronic acid (3 mg/ml). Transglutaminase and thrombin were used as crosslinking agents. 2 ml bioink was mixed 500 µl of ACL cells (1×10^6 - 4×10^6 per ml) from two different donors and the cell laden ink was printed by 150 µm nozzles. As a control, the hydrogel was printed and ACL cells were seeded on the printed structures to monitor the bioprinting process effect on the cell viability. The viability of printed cells was examined using calcein-ethidium homodimer

dyes under the LSM710 confocal microscopy and Alamar Blue at four different time points.

Results

The printed constructs were cultured for 14 days. The viability and cell activity of ACL cells were analyzed on Day 1, Day 3, Day 7 and Day 14. High cell viability was observed for both the seeded and printed ACL cells group as seen Figure 1. The seeded cells were “happier” than the printed cell in the beginning of incubation time. However, the printed cells were happier than the seeded cells after 14 days incubation.

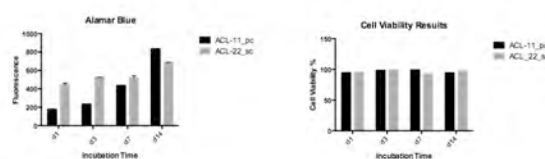


Figure 1: Alamar blue and cell viability results of bioprinted and seeded cells

Discussion

In this work, we describe the development, optimization of a 3D bioprinted ACL scaffolds and determinate an appropriate printing parameter with respect to cellular response and mechanical properties. To this end, this study examined the effect of the printing process and the attachment and proliferation of primary human ACL cells. The results showed that the viability of cells was not affected by the printing process. Future work will involve also the usage of primary intervertebral disc cells in order to test applications on microfluidic chip.

References

1. Gantenbein B, Gadhari N, Chan SC, Kohl S, Ahmad SS. Mesenchymal stem cells and collagen patches for anterior cruciate ligament repair. *World Journal of Stem Cells* (2015).

FINITE ELEMENT SIMULATION FOR 3D PRINTED SCAFFOLDS

Xiuyu. Wang (1,3), Paul F. Egan (1), Kristina A. Shea (2), Stephen J. Ferguson (1)

1. Institute for Biomechanics, ETH Zurich, Switzerland 2. Engineering Design and Computing Laboratory, ETH Zurich, Switzerland 3. Cardiovascular and Cellular Engineering Lab, Ecole Polytechnique, France

Introduction

Finite element simulations (FEM) are able to improve the efficiency of design automation of lattice scaffolds for spinal fusion cage applications [1]. With computational simulation, scaffolds optimized with discrete beam elements may be designed with favorable mechanical and structural properties prior to validation with mechanical loading tests. Several design parameters may influence mechanical performance of the scaffold, such as porosity, beam diameter, lattice topology and number of cell units [2]. Different scaffold types are studied to determine trade-offs in how unit cells may influence performance (Fig. 1).

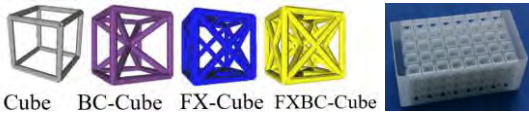


Figure 1 Scaffold topology types, Cage with BC-Cube

Methods

FEM simulations are conducted to predict the mechanical properties based on the lattice's porosity [3]. Porosity is a measure of void space in scaffold. While maintaining mechanical strength of the scaffold, design automation should maximize porosity in order to facilitate a higher volume of tissue growth.

In the simulation, a quasi-static displacement is applied on the top of scaffold and stops at 20% of the scaffold length. In this study, it focuses on the Stress-Strain Curve of elastic modulus of scaffolds of different porosity and topology types. Reaction force and displacement are also measured.

To compare the results, in each simulation group the parameters are set by controlling variable values. Some variables are coupled, such as different porosities resulting in corresponding unit cell length (Table 1). When porosity is modified, unit cell length should be updated simultaneously. All lattices have three unit cells along each axis for a total 27 unit cells.

Porosity	50%	65%	80%
Cell Length [μm]			
Cube	2070	2700	3880
FX-Cube	3850	4960	7000
BC-Cube	3260	4130	6000
FX-BC-Cube	4750	6050	9000

Table 1: Unit cell design for different porosity

Results

Scaffold stiffness is inversely proportional to its porosity, as shown in Figure 2

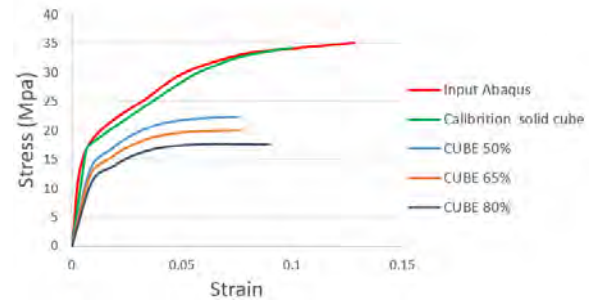


Figure 2 Stress Strain Curve of Cube

By controlling porosity fixed at 65% and beam diameter at 800 μm, varied cell topologies showed different loading performances (Fig. 3). For the same pre-condition, Cube is the stiffest design. All other types have similar stiffness. Since other structures have more beams in diagonal, they have less material aligned with the loading direction, making them less stiff for this compressive case.

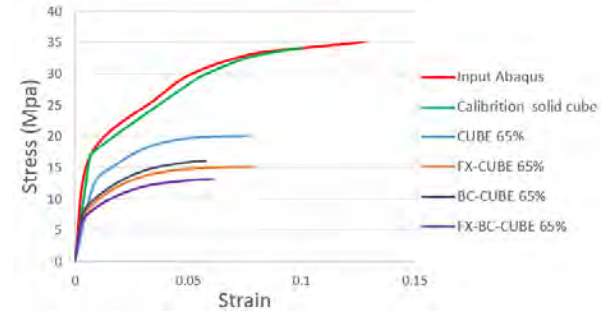


Figure 3 Stress Strain Curve of different cell types

Discussion

For future work, some developed simulation, such as cage performance between two vertebrae, will be conducted. The simulation enable us to compare the performances of different scaffold theoretically and could provide evaluations for improving designs. Mechanical experiments are required for validating simulation predictions and testing the complete cage.

References

- Egan Ferguson, K. Shea, J M Des 139.6: 061401, 2017.
- Lee, Yung-Heng et al., Com Bio Med 71: 35-45, 2016
- Habib, Fatah et al., 3DP Add Manu 3.2: 119-127, 2016

ADVERSE IMMUNE EFFECTS TO ARTIFICIAL, SHEAR-RESPONSIVE LIPOSOMES

Sofiya Matviyiv (1), Marzia Buscema (1), Tamás Mészáros (2,3), Gabriela Gerganova (1), Thomas Pfohl (1), Andreas Zumbuehl (4), János Szebeni (2,3), and Bert Müller (1)

1. Biomaterials Science Center, University of Basel, Switzerland; 2. Nanomedicine Research and Education Center, Semmelweis University, Hungary; 3. SeroScience Ltd., Hungary; 4. Department of Chemistry, University of Fribourg, Switzerland;

Introduction

Liposomes are one of the most successful drug delivery nanosystems, which increases therapeutic index of incorporated medicines and improves their delivery to the targeted tissue. Since their discovery in 1965 [Bangham, 1965], various stimuli-responsive liposomes were developed [Mura, 2013]. Recently, the mechano-responsive Pad-PC-Pad liposome was discovered [Holme, 2012]. Their capability of drug release at increased shear stress makes Pad-PC-Pad liposomes a promising candidate for first-line treatment of atherosclerosis. The wall-shear stress at critically stenosed arteries is at least an order of magnitude higher than under healthy conditions [Saxer, 2013]. Therefore, it can be used as a purely mechanical trigger to release a vasodilator drug preferentially at the sites of constriction.

Liposomes, however, can cause adverse reactions, which involves many organ systems [Szebeni, 2012]. Often these reactions arise from activation of complement system. The European Medicines Agency recommends *in vitro* and *in vivo* assessments of complement reactions in sensitive animal models as a preclinical assay in the development of liposomal drugs [E.M.A., 2013]. Consequently, we determined the concentration of specific complement complexes, which are responsible for the activation of the complement cascade by liposomal drugs.

Methods

Three Pad-PC-Pad liposomal formulations (A: Pad-PC-Pad/DSPE-PEG2000 + NTG; B: Pad-PC-Pad/DSPE-PEG2000 + saline; C: Pad-PC-Pad + NTG) were prepared as described previously [Matviyiv, 2017]. The size of the liposomes was measured by dynamic light scattering. The phospholipid content of the samples was determined by the phosphate test 2.0 [Stalder, 2013]. To detect the adverse reactions, human sera were tested using MicroVue C4d, Bb, SC5b-9 ELISA kits.

Results

The phospholipid content of the formulations ranged between (8.2 ± 1.0) and (10.3 ± 0.4) mg/ml.

The size of liposomes was for L1 (131 ± 4) nm, for L2 (116 ± 1) nm, and for L3 (2660 ± 250) nm. Concentrations of C4d and Bb proteins were examined to determine the pathways in the activation cascade.

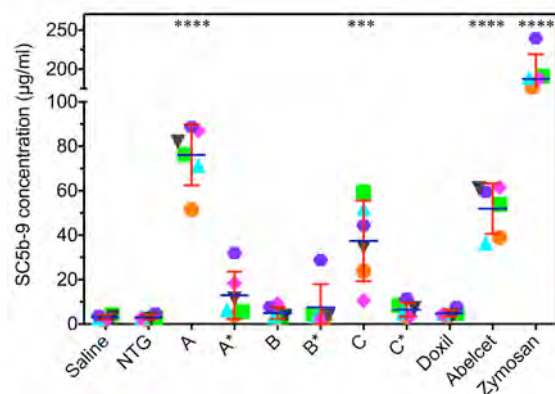


Figure 1 Level of activated SC5b-9 complex. Data are shown as the values of six sera and error bars as the standard deviation among the individuals. Significance of differences among the groups was determined by an ordinary one-way ANOVA, followed by Dunnett's multiple comparison test ($P < 0.05$).

Discussion

The classical pathway can be excluded for the shear-responsive Pad-PC-Pad liposomes. The formation of SC5b-9 complex was determined and to some extent, all formulations induced the formation of an SC5b-9 complex. Nevertheless, liposomal samples containing relevant therapeutic dose of nitroglycerin do not induce significant complement activation *in vitro* with human sera, unlike Abelcet, the FDA-approved amphotericin B phospholipid complex, that triggered three-fold increased reaction.

References

- Bangham et al, J Mol Biol 13:238-IN27, 1965.
- European Medicine Agency, Rev 02, 2013.
- Holme et al, Nat Nanotechnol 7:536-543, 2012.
- Matviyiv et al, Proc of SPIE 10162:101620A-1, 2017.
- Saxer et al, Cardiovasc Res 99:328-333, 2013.
- Szebeni et al, Eur J Nanomed 1:33-53, 2012.

CHARACTERIZATION OF SHEAR-RESPONSIVE LIPOSOMES USING MICROFLUDICS AND SMALL-ANGLE X-RAY SCATTERING

Thomas Pfohl (1), Marzia Buscema (1), Sofiya Matviyiv (1), Hans Deyhle (1),
Simone E. Hieber (1), Andreas Zumbuehl (2), Bert Müller (1)

1. Biomaterials Science Center (BMC), University of Basel, Gewerbestrasse 14, 4123 Allschwil, Switzerland; 2. Department of Chemistry, University of Fribourg, Chemin du Musée 9, 1700 Fribourg, Switzerland

Introduction

Recently, shear-responsive and biocompatible liposomes were introduced as possible drug delivery systems for the treatment of myocardial infarction [Holme et al., 2012]. In order to analyze the shape and structural changes of these lipid-based nano-containers under hydrodynamic stimuli, small-angle X-ray scattering (SAXS) was combined with microfluidics [Koester & Pfohl, 2012]. The microfluidic devices were designed to mimic the hydrodynamics and effective shear stresses found in healthy and stenosed regions of coronary arteries [Buscema et al, 2016].

Methods

Flexible and reproducible microfluidic devices were fabricated using soft lithography and consisted of poly(di-methyl-siloxane) (PDMS), UV-curable adhesive material, and polyimide foils [Koester & Pfohl, 2012]. The spatially resolved SAXS measurements were carried out at the cSAXS beamline (Paul Scherrer Institute, Swiss Light Source, Villigen, Switzerland) using a scanning setup with a photon energy of 12 keV, a beam size of $40 \times 40 \mu\text{m}^2$ and a sample-detector distance of 2.2 m.

Results

A microfluidic device mimicking a stenosed blood vessel was scanned in two orthogonal directions across the X-ray beam to acquire spatially resolved SAXS data. With this setup, we were able to obtain structural and shape information about the liposomes under pre-selected flow conditions (see Figure 1). Analyzing the structure and shape of the liposomes at positions of interest within the microfluidic device, we have found an orientation along the streamlines as well as a small anisotropy of the scattering signal at the transition from the wider to the constricted areas of the micrometer-sized channels – emulating healthy and diseased blood vessel geometries.

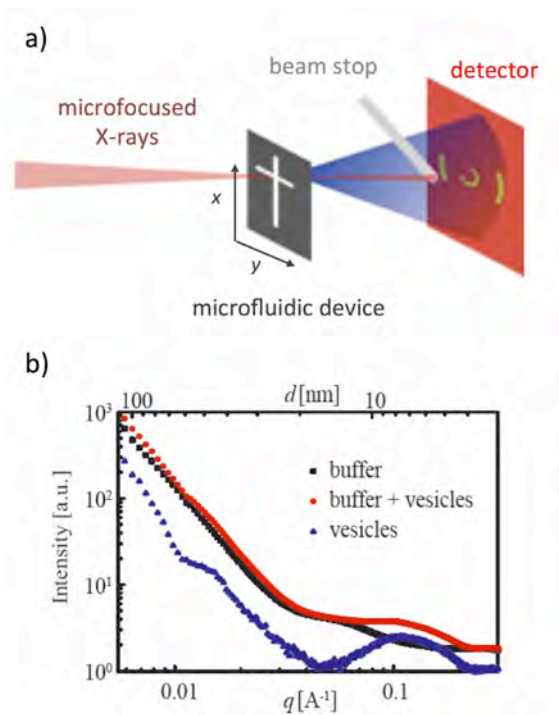


Figure 1: a) Schematic representation of a combined micro-fluidics and micro-focused SAXS setup. b) SAXS profiles of a liposome suspension, a buffer solution, and their difference profile in the micro-fluidic device.

Discussion and Conclusions

SAXS combined with microfluidics is a valuable tool to determine the structural and shape changes of liposomes under realistic hydrodynamic conditions, as one finds in diseased, stenosed human arteries.

Acknowledgements

We gratefully acknowledge the allocated beamtime at the cSAXS beamline at Swiss Light Source, PSI, Villigen, Switzerland.

References

- Holme et al, Nat Nanotech, 7:536-543, 2012.
- Koester & Pfohl, Mod Phys Lett B 26:1230018, 2012.
- Buscema et al, Proc of SPIE 9797:97970S, 2016.

TEMPLATE STRIPPING BASED NANOTRANSFER PRINTING OF PLASMONIC GOLD STRUCTURES FOR BIOSENSING APPLICATIONS

Raphael F Tiefenauer, Klas Tybrandt, János Vörös

Laboratory of Biosensors and Bioelectronics, ETH Zurich, Switzerland.

Nanostructures are promising transducers for novel biosensing concepts, especially for point-of-care diagnostics. Plasmonic gold nanostructures, for example, enable label-free sensing based on localized surface plasmon resonance (LSPR). However, the fabrication of such structures is mostly limited to small areas, costly, and requires harsh fabrication conditions.

We developed a sub-50 nm fabrication technique overcoming those current limitations. The template-stripping-based nanotransfer printing technique only requires one reusable mold, thus multiplying the number of structures.

This versatile technique enables the transfer of arbitrary thin film metal structures onto a variety of substrates including glass, silicon, PDMS, and SU-8. Thus the process is also suitable for stretchable electronics. Additionally, structures can be transferred onto curved substrates and the technique is compatible with roll-to-roll fabrication. Hence, this method is attractive for industry scale production. Structures can range from tens of nanometers to hundreds of micrometers over a wafer scale area (see Figure 1). The process, which only takes minutes, is solvent-free and also enables multiple layers. The stability of transferred gold structures on glass exceeds by far those fabricated by e-beam evaporation. An adhesion layer is no longer needed, enabling a faster, cheaper fabrication, as well as the production of superior plasmonic structures.

We believe that this simple, cost efficient, and fast method to fabricate robust nanostructures is not only limited to biosensors, but also has potential in the development of transistors, metamaterials, epidermal sensors and other emerging devices.

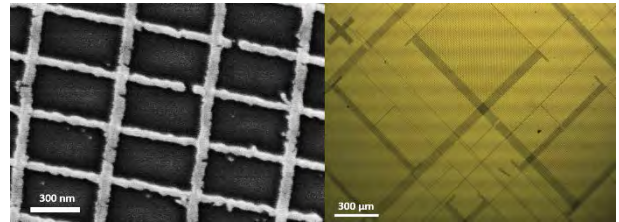


Figure 1: Transferred gold structures on glass. (a) Two layers of 10 nm thin nanowire arrays (60 and 80 nm wire widths). (b) Two layers of 100nm thick test structures (1 - 2000µm features).

FABRICATION OF NANO-STRUCTURED DIELECTRIC ELASTOMER TRANSDUCERS FOR MEDICAL IMPLANTS

Tino Töpper, Bekim Osmani, Matej Siketanc, and Bert Müller

Biomaterials Science Center, Department of Biomedical Engineering, University of Basel, Gewerbestrasse 14, 4123 Allschwil Switzerland

Introduction

Currently available dielectric elastomer transducers (DETs) exhibit limits regarding their processability, which hinders a breakthrough towards low-voltage operation. Recently, however, first results on nanometer-thin silicone membranes for low-voltage DETs have been published [Töpper, 2015]. Creating homogeneous films of high-permittivity elastomers as thin as one micrometer still presents a challenge for realizing the entire spectrum of applicability of DETs as sensors, actuators, and even energy harvesters for smart and autonomous medical implants. Herein, we compare in-house built PDMS thin-film fabrication (setups?) techniques: organic molecular beam deposition (OMBD) and electro spray deposition (ESD) with respect to deposition rates, surface roughness and minimal film thicknesses to obtain confluent layers.

Methods

The fabrication of DETs using OMBD is schematically shown in Figure 1. The thickness is monitored using real-time spectroscopic ellipsometry (SE801, Sentech, Berlin, Germany) with SpectraRay3 software.

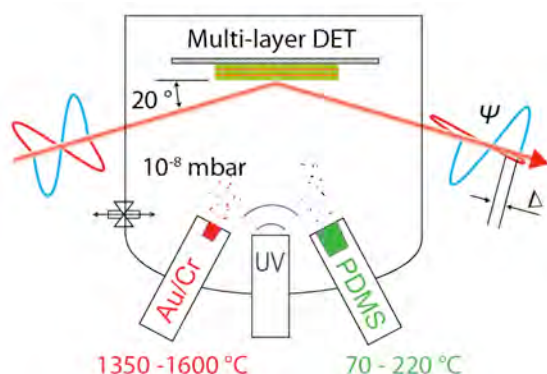


Figure 1: Fabrication of DETs using organic molecular beam deposition (OMBD).

PDMS (V05/V21, Gelest, Inc., Morrisville, PA, USA) was evaporated using a low-temperature effusion cell ((NTEZ, Dr. Eberl MBE Komponenten GmbH, Weil der Stadt, Germany) and deposited under ultra-high vacuum conditions. Au and Cr (Kurt J. Lesker Company, UK) were evaporated using a high temperature effusion cell. DETs were grown on 2-inch Si wafers (SIEGERT WAFER GmbH, Aachen, Germany).

The fabrication of DETs using ESD is schematically shown in Figure 2. PDMS (GP-367, Genesee Polymers Corporation, USA) was dissolved in ethyl acetate and sprayed at a rate of 10 $\mu\text{l}/\text{min}$. An alternating voltage signal (Tektronix AFG3021C, Linktronix AG, Thalwil, Switzerland) was amplified to $\pm 5 \text{ kV}$ using a high voltage power amplifier (TREK 10/40A, TREK INC., Lockport, NY, USA). PDMS films were crosslinked using a UV lamp (L2423, Hamamatsu Photonics, Japan).

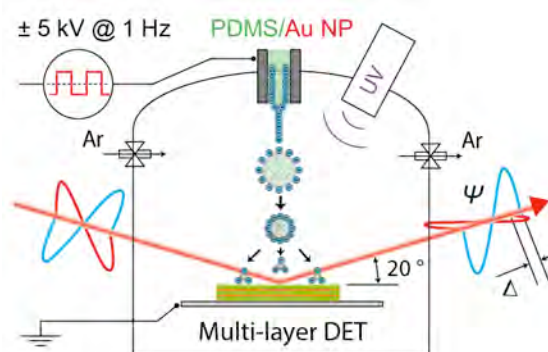


Figure 2: Fabrication of DETs using electro spray deposition (ESD).

Results and Discussion

The evaporation of PDMS using OMBD is limited to oligomers and shows low deposition rates [Töpper, 2016]. ESD is 10 \times faster and allows for upscaling [Osmani, 2017]. The main parameters are summarized in Table 1.

	OMBD	ESD
Roughness on Si (nm)	1	1
Growth rate (nm/min)	5	500
Min. film thickness (nm)	>20	>200
Molecular weight (g/mol)	<6'100	<60'000
Processing temp. ($^{\circ}\text{C}$)	~ 214	~ 20

Table 1: Comparison between OMBD and ESD

Acknowledgements

The financial contributions of the nano-tera.ch initiative and the Swiss Nanoscience Institute (SNI) for the AFM is gratefully acknowledged.

References

- Töpper *et al.*, *Sens. Actuators A* **233**, 32-41, 2015.
- Töpper *et al.*, *APL Mater.* **4**, 056101, 2016.
- Osmani *et al.*, *Proc. SPIE* **10163**, 101631E, 2017.

LUNG MICROVASCULATURE-ON-CHIP: IN VITRO MICROFLUIDIC PLATFORM FOR DRUG TESTING

Soheila Zeinali (1), Colette A. Bichsel (2), Nina Hobi (1), Manuela Funke (3,4), Olivier T. Guenat (1,3,5), Thomas Geiser (3,4)

1. *Organs-on-Chip Technologies Laboratory, ARTORG Center, University of Bern, Bern, Switzerland*; 2. *Vascular Biology Program, Boston Children's Hospital, Harvard Medical School, Boston, MA, USA*; 3. *Department of Pulmonary Medicine, University Hospital of Bern, Bern, Switzerland*; 4. *Department of Clinical Research, University of Bern, Bern, Switzerland*; 5. *Division of General Thoracic Surgery, University Hospital of Bern, Bern, Switzerland*

Introduction

Differences in cellular responses observed in standard in vitro studies, animal models, and human clinical studies, decrease efficiency of developing new therapeutic strategies. This is specifically true for the organs of huge complexity, heart and lung where the function of each involves physical forces and varies with species, age, and state of health. Recent studies have shown the feasibility of in vitro self-assembled perfusable microvessel networks [Kim, 2013]. Such models hold several features of in vivo vascular microenvironment. Based on in vitro vasculogenesis model using co-culture of endothelial cells (EC) and pericytes, Bichsel et al., described the biomimetic model of lung parenchyma microvasculature. This microfluidic co-culture system enabled the formation of the microvessel network that resembled human lung microvasculature in terms of morphology, vascular marker expression, permeability, and vasoactive response [Bichsel, 2015]. By reproducing specific physiological functions, in vitro tissue models own capability to investigate the efficacy, toxicity and mode of action of therapeutic agents. The aim of this study is to explore the mode of action of nintedanib, the drug agent used for the treatment of idiopathic pulmonary fibrosis (IPF), on in vitro human lung microvasculature architecture. The anti-angiogenic efficacy of nintedanib in treatment of IPF is studied in the literature, but needs more investigations to clarify the mechanism of angiogenesis and vasculogenesis inhibition.

Methods

We studied the efficacy and action of nintedanib on in vitro human lung microvasculature, by investigating vasculogenesis within a 3D fibrin scaffold by co-culturing ECs and lung fibroblasts (Fb). The system is a 100 μm -in-height microfluidic platform with five compartments, one central chamber for co-culturing EC and Fb, two side chambers for mono-culturing Fb and two microchannels for medium supplying. To observe the effect of the drug, different concentrations of nintedanib in cell culture medium were investigated.

Results

The microvasculature-on-chip model provides the possibility to study the effect of nintedanib on permeability, perfusability and vascularized area of a human lung microvasculature model. The anti-vasculogenesis impact of nintedanib is significant for concentrations starting at 10nM, with an increase in vessel permeability coefficient and decrease in vessel density.

Discussion

As a replacement to animal models, advanced in vitro microvasculature-on-chip could open new prospects to study the mode of action of therapeutic compounds, such as nintedanib. Experimental platforms, such as this one, can address fundamental questions of drug effects on angiogenesis and vasculogenesis, and can be used to optimize drug treatments on personalized vasculature models.

References

- S. Kim et al, Lab on a chip, 13: 1489–500, 2013.
- C. A. Bichsel et al, Tissue Engineering - Part A, 21: 2166–2176, 2015.

Development of a lung alveoli array-on-chip with a collagen-elastin membrane

Pauline G.V. Zamprogno¹, Sven Achenbach¹, Janick D. Stucki¹, Nina Hobi¹, Nicole Schneider-Daum², Claus-Michael Lehr², Hanno Huwer³, Ralph A. Schmid⁴, Olivier T. Guenat^{1,4,5}

1. *Organs-on-Chip Technologies Laboratory, ARTORG Center for Biomedical Engineering Research, University of Bern, Bern, Switzerland* 2. *Drug Delivery (DDEL), Helmholtz-Institute for Pharmaceutical Research Saarland (HIPS), Saarbrücken, Germany* 3. *SHG Clinics, Department of Cardiothoracic Surgery, Völklingen Heart Center, Völklingen, Germany* 4. *Division of General Thoracic Surgery, University Hospital of Bern, Bern, Switzerland* 5. *Department of Pulmonary Medicine, University Hospital of Bern, Bern, Switzerland*

Introduction

Standard *in vitro* lung alveoli models poorly reproduce the microenvironment of the distal airways. Recently reported, advanced *in vitro* models, called lung-on-chips, reproduce the air-blood barrier including the cyclic stress of the breathing movements [1], [2]. However, they are made of a polydimethylsiloxane (PDMS) membrane, whose chemical and physical properties differ by far from those of the alveolar basal membrane.

The goal of the project is to develop an array of tiny lung alveoli with physiological dimensions, equipped with a stretchable biological membrane made of extracellular matrix (ECM) proteins instead of PDMS.

Material & Methods

We develop a new membrane made of collagen and elastin, two main components of the basal membrane, which provide the elasticity to the tissue. The membrane is supported by a hexagonal gold mesh, which mimics the physiological dimension of the lung alveoli.

For the development of the alveoli model, we used human alveolar type II cells from patient provided by the N. Daum group. The cell isolation and the seeding procedure that followed, is described in [3]. After 48h, cells can be cultured at the air-liquid interface (ALI). Primary lung endothelial cells are from Angiocrine Bioscience (Veravec).

Results

The newly developed biological membrane is porous and stretchable. It allows the development of an *in vivo*-like lung alveoli model, with a monolayer of type II (ATII) and type I (ATI) like cells in co-culture with endothelial cells (figure 1a and 1b). This model is stable for at least three weeks. The primary cells form a tight barrier (figure 1c), and they express markers of tight junction even at ALI condition (figure 1d).

Preliminary results demonstrate that the lung alveoli model can be cultured for several days under cyclic stress.

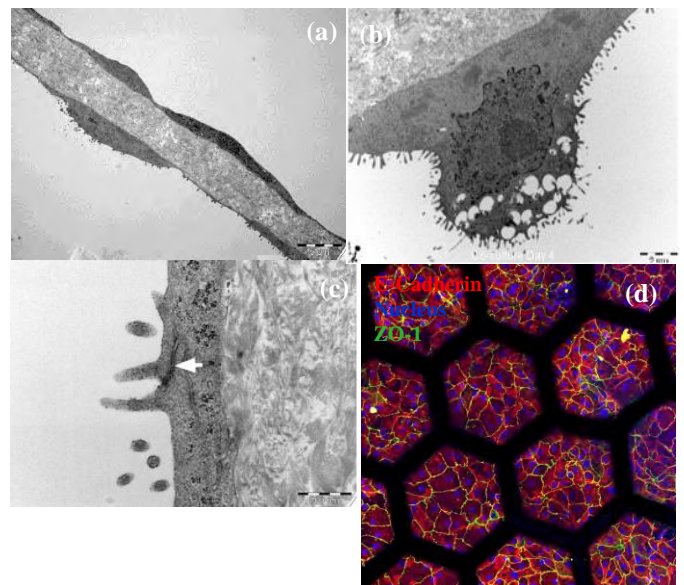


Figure 1: Lung alveoli *in vitro* model on a collagen-elastin membrane. (a) Co-culture of ATI like cells with endothelial cells (VeraVec), TEM, day 4; (b) ATII like cells, TEM, day 4; (c) Tight junctions between ATI like cells in co-culture with VeraVec, day 2; (d) Barrier formation of alveolar cells in monoculture at ALI, day 4.

Discussion

This new advanced model mimics the composition, dimensions, and mechanical stretch of the lung alveoli. The long-term stability of the membrane and its entirely biological nature makes this model a promising tool for drug discovery.

Acknowledgements

We thank Beat Haenni for his help in the acquisition of TEM pictures.

References

- [1] D. Huh et al., *Science*, 328:1662-1668,2010
- [2] A. O. Stucki, J.D. Stucki et al., *Lab Chip*, 15:1302-1310,2015
- [3] S. Fuchs et al., *Cell Tissue Res*, 311:31-45,2003

AN INTEGRATED ELECTROSPRAY GENERATOR FOR GENE DELIVERY

Claudio Minonzio (1), Amiq Gazdhar (2), David Hradetzky (1)

1. University of Applied Sciences Northwestern Switzerland, School of Life Sciences, Institute for Medical and Analytical Technologies
2. University of Bern, Department of Clinical Research

Introduction

Targeted delivery of plasmids or drugs will be a key technology for clinical application of gene therapy. Gene delivery devices have to enable the penetration of the plasmid into the interior of cells, while avoiding residual cell damage. The electrospray process utilizes an electrical field to generate an aerosol of the plasmid to accelerate it towards the targeted tissue and facilitates the plasmid to enter cells. Therefore, high electrical potential difference between a capillary and a counter electrode is required [Hradetzky, 2012]. In order to enable electrospray within clinical surrounding, a generator is required, providing a predefined application protocol by adjusting applied electrical voltage and delivery of liquid drugs in terms of flow rate and volume through the capillary. Goal of presented work is the concept and realization of a fully automated easy-to-use integrated device with one-touch functionality for in vitro research first.

Methods

For well-defined delivery of plasmid solution, a syringe pump module is used to deliver the liquid to the tip of the capillary. Additionally the capillary acts as working electrode, where a high voltage module is connected. Working current is limited to 50 μ A and continuously monitored.

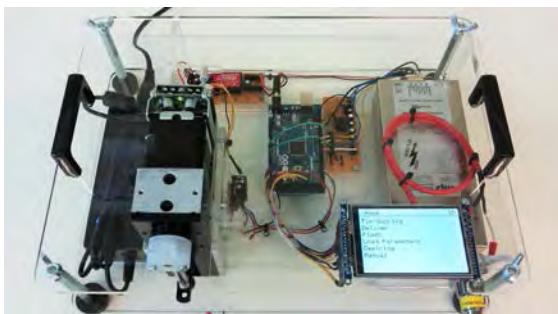


Figure 1: The developed system is an all-in-one device

Both commercial available modules are controlled using a microcontroller (μ C). For easy-to-use operation of the electrospray generator, a touch-screen is integrated, providing a context sensitive graphical user interface (GUI).

Results

Core element of the generator is the μ C (Mega 2560). The syringe pump (Hamilton PSD/4 with 3/2 way valve and 250 ml syringe) is driven by a simple R232 interface implemented, enabling delivery of predefined volume (25 μ l) and flow rates (20 μ l/min). The HV-module (Iseg DPR 60 155 24 5 EPU, +/- 0.5-6 kV) is interfaced by an analog interface, and controls the voltage applied to capillary. The output of the HV-module of driving current and voltage is monitored, acting as feedback loops of the electrical system, and enables interrupt of the automated process controlled by the μ C.

For simple interaction, predefined sequences for delivery of drugs, two modes for loading the system with drug solution, and flushing the system are implemented, and may be selected through the GUI (Adafruit 3.5" Color TFT Breakout). Loading the system may be realized either from the tip for small volumes or fully preloaded for repeated sequential application. The delivery process itself requires a protocol for establishing and monitoring the electrical power first, starting the delivery process through the pump second, delivering a predefined volume at predefined flow rate third, stopping the delivery process fourth, and decreasing the electrical power with a delay in time (7.5 sec) fifth. In any case, electrical current exceeding the predefined limit will result in a decrease of electrical voltage. In any of described operation modes, the user may interrupt or stop the process. All predefined parameters are stored in an integrated SD card.

Discussion

A fully automated device with a one-touch function for easy use has been realized. The user and patient safety is guaranteed by constant monitoring of voltage and current. The restricted changing of parameters via the SD card ensures the quality of the experiments

References

- D. Hradetzky, S. Boehring, T. Geiser, and A. Gazdhar, "An approach towards bronchoscopic-based gene therapy using electrical field accelerated plasmid droplets," Conf Proc IEEE Eng Med Biol Soc, vol. 2012, pp. 5753-6, 2012.